nature portfolio

https://doi.org/10.1038/s41586-023-06381-1

Supplementary information

A heavyweight early whale pushes the boundaries of vertebrate morphology

In the format provided by the authors and unedited

Supplementary information

A heavyweight early whale pushes the boundaries of vertebrate morphology

Supplementary Methods

SM, dry skeletal mass; SF, skeletal fraction; BM, total body mass.

Geological and palaeoenvironmental setting

The Pisco Basin is a NW-trending Andean forearc basin that extends along the coastal plain of southern Peru, between the towns of Pisco and Nazca. Here, the aseismic Nazca Ridge impinges on the Peru–Chile trench, causing the uplift of the eastern portion of the basin fill[1–4] (Extended Data Fig. 5a). The latter is extensively exposed throughout the Ica desert in the form of a Cenozoic succession of mostly marine deposits that comprises, from older to younger, the lower Paleogene Caballas Formation, the Eocene Paracas Formation, the Eo–Oligocene Otuma Formation, the Lower Miocene Chilcatay Formation and the Mio–Pliocene Pisco Formation[5–8]. These sedimentary units are lithologically complex as well as bounded by regionally extensive unconformities that reflect periods of subaerial exposure and non-deposition[6,8–10]. Except for the Caballas Formation, whose outcrops are limited to the southern portion of the basin, the aforementioned units can be grouped into two different megasequences (Di Celma et al., 2022), the oldest of which (megasequence P, consisting of the Paracas and Otuma formations) is exposed at the study site.

Comprising the base of megasequence P, the Paracas Formation consists of a coarse-grained lower portion (the Los Choros member, made of conglomerates and mixed siliciclastic-bioclastic sandstones with abundant tests of large benthic foraminifera) that is topped by a division of finer deposits (the Yumaque member, consisting of silty sandstones and siltstones that host a rich planktic assemblage)[6,11–16]. During sedimentation of the Los Choros strata, the palaeoenvironment was tropical, shallow-marine and very close to a rocky shore, whereas the Yumaque was deposited in a deeper and more distal setting and records the onset of a cooling trend at about 38 million years ago (Ma)[15–17]. Biostratigraphic analyses indicate that the Paracas Formation deposited from the Lutetian throughout the Bartonian to the Bartonian–Priabonian transition (Extended Data Fig. 5b). At and around Zamaca, deposition of the Los Choros member started around 43.6 Ma[15], whereas the Yumaque member deposited between 42.37 and 37.88[16]. The Otuma Formation is formed by a basal package of sandstones that passes upward into alternating siltstones and diatomites, the latter being home to common pelagic microfossils and fish debris[6,13,16]. These strata testify to a temperate palaeoclimate and moderate upwelling, with seawater temperatures decreasing and nutrient availability increasing up section[16]. Biostratigraphic studies performed at Zamaca indicate that the Otuma beds cropping out in this area are Priabonian in age, their base and top being dated at about 37 Ma and ca. 35–34 Ma[16]; elsewhere in the basin, the uppermost strata of the Otuma Formation extend into the Oligocene[18] (Extended Data Fig. 5b).

At the *Perucetus colossus* type locality, the Yumaque–Otuma transition has a relatively subtle lithological expression and has been identified herein on a biostratigraphic basis; calcareous nannofossil bioevents indicate that the type horizon belongs to the upper portion of the Yumaque member (compare Malinverno et al.[16]). The beds that yielded the cetacean bones consist of finely laminated mudstones. Macrofossil remains from these deposits include rare small bivalves (most of which are preserved as inner moulds), carbonified plant remains and fish debris. The latter are largely comprised of scales of Carangidae, Clupeidae, and Scombridae (Giorgio Carnevale, pers. comm., 2022). The thoroughly laminated mudstones suggest deposition in a low-energy setting. At the same time, the occurrence of conglomeratic intervals (interpreted herein as tempestites) and abundant *Gyrolithes* burrows a few metres below the *P. colossus* holotype (Extended Data Fig. 5c) suggests that the

depositional setting was not far from the coast[19]. As such, the available sedimentological and paleontological evidence point to deposition below the storm wave-base in relatively quiet, deep-water settings similar to those found in a proximal offshore zone. The abundant occurrence of fish remains belonging to three families of quintessentially pelagic teleosts suggests a frankly marine, open-sea setting, as also evoked by the abundance of calcareous nannofossils and the lack of typically coastal genera (*Micrantholithus*, *Pemma*, *Zygrhablithus*) found instead at the base of the Yumaque member; at the same time, the common occurrence of macroscopic plant remains suggests strong connections with terrestrial/marginal-marine environments.

Whereas cool water conditions were inferred for the Yumaque member by Uhen et al.[14], subsequent works[15–17] have reconstructed the Yumaque palaeoenvironment as overall warm-temperate. That said, the upper portion of the Yumaque strata records a distinct change in nannoplankton assemblages around 38 Ma, likely reflecting the beginning of a cooling trend in the framework of global climate change and/or the development of a weak upwelling system[16]. As the *P. colossus* holotype dates back to 39.8-37.84 Ma, and probably closer to the latter date, it may either precede or be roughly coeval to the aforementioned cooling event. At that time, the East Pisco Basin was characterised by relatively high values of ocean primary productivity[16].

Biostratigraphy

Calcareous nannofossils are rare to common through the stratigraphic section of the type locality of *Perucetus colossus*, but they are absent in a few intervals; their preservation ranges from bad to moderate to good. The base of the section is in the Yumaque member of the Paracas Formation and is above the FO of *Reticulofenestra stavensis* (FO 40.34 Ma) within zones NP16 / CNE15-16 (Extended Data Fig. 5). The LO of *Sphenolithus spiniger* occurs 1.5 m above the base of the section: although this bioevent is considered as time-transgressive (LO between 40.1-37.3 Ma), it is well constrained in the area of the Rio Ica[16], where it occurs 20-25 m above the FO of *R. stavensis*. The LO of *Chiasmolithus solitus* (39.8-38.7 Ma) occurs at 10 m and marks the transition to zone NP17. *Reticulofenestra reticulata* displays an increase in abundance in this interval: this is a local event that is typically identified within the interval of LO of *S. spiniger* and *C. solitus* in the Ica River area (Malinverno et al., 2021). The FO of *Chiasmolithus oamaruensis* (37.84 Ma) occurs at 31 m, one metre above the *P. colossus* skeleton. This species is extremely rare in the Rio Ica area, but its presence has been previously identified in the uppermost layers of the Yumaque member of the Paracas Formation and as such, can serve as a local correlation event[16]. One single specimen of *Reticulofenestra erbae* (37.88-37.46 Ma) is identified 20 cm below: this species is extremely rare in the area, but its presence indicates the occurrence of zone CNE17. Another local event is represented by the LO of *Neococcolithes*, which occurs at 33.5 m and, in the other sections of the Ica River area, marks the top of the Yumaque member.
Above the base of the Otuma Formation, the FO of *Isthmolithus recurvus* (FO 36.84 Ma) occurs at 37 m and marks the transition to NP19-20 within CNE18. Above this interval, the increase in abundance of *Pontosphaera multipora* is also recognised, as a local event of correlation to the other sections of the Ica River area[16].

^{39}Ar–^{40}Ar dating on tephra

The ash sample results in at least 95% of volcanic components (glass shards and phenocrysts), which is consistent with the fact that tephra is the result of primary deposition[20–22]. Phenocrysts are ca. 5% and are composed of biotite with glass and apatite inclusions, quartz, and feldspars (Fig. S1a,b).

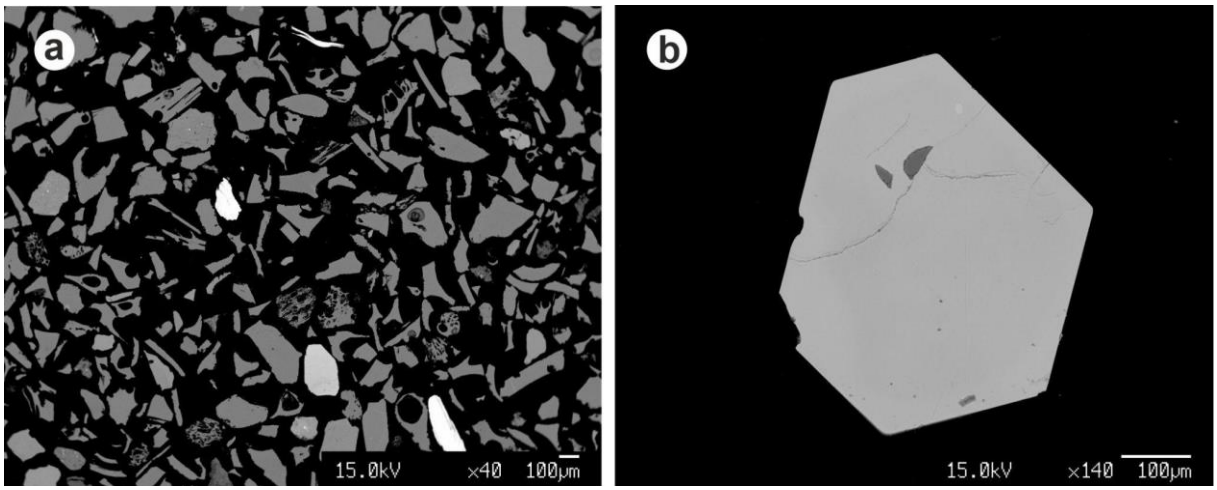

Figure S1. a. BSE image of the 250-µm-size fraction of the dated volcanic ash. **b.** BSE image close-up of a well-preserved biotite crystal with glass inclusions. To obtain statistically significant results, the EPMA analyses were performed on 20 glass shards as well as on 10 biotite crystals (both rim and core).

Glass shards display a bubble-wall and low vesiculated morphology (Fig. S1b). Grain-size analysis reveals a bimodal ash belonging to the textural group of "sandy silt", composed of 63% silt, 35% sand, and 2% clay (Fig. S2).

a

SAMPLE TYPE: Bimodal, Very Poorly Sorted
SEDIMENT NAME: Very Fine Sandy Very Coarse Silt
TEXTURAL GROUP: Sandy Mud

	µm	ϕ
MODE 1:	84.48	3.568
MODE 2:	7.529	7.056
MODE 3:		
D_{10}:	3.857	2.797
MEDIAN or D_{50}:	34.47	4.859
D_{90}:	143.8	8.018
(D_{90} / D_{10}):	37.30	2.866
(D_{90} - D_{10}):	140.0	5.221
(D_{75} / D_{25}):	9.235	1.906
(D_{75} - D_{25}):	76.67	3.207

GRAIN SIZE DISTRIBUTION

GRAVEL: 0.0%	COARSE SAND: 0.0%
SAND: 34.8%	MEDIUM SAND: 0.9%
MUD: 65.2%	FINE SAND: 12.8%
	V FINE SAND: 21.1%
V COARSE GRAVEL: 0.0%	V COARSE SILT: 17.3%
COARSE GRAVEL: 0.0%	COARSE SILT: 13.7%
MEDIUM GRAVEL: 0.0%	MEDIUM SILT: 12.3%
FINE GRAVEL: 0.0%	FINE SILT: 11.7%
V FINE GRAVEL: 0.0%	V FINE SILT: 8.0%
V COARSE SAND: 0.0%	CLAY: 2.2%

	METHOD OF MOMENTS			FOLK & WARD METHOD		
	Arithmetic µm	Geometric µm	Logarithmic ϕ	Geometric µm	Logarithmic ϕ	Description
MEAN ($\bar{x}$):	56.46	27.79	5.169	28.06	5.156	Coarse Silt
SORTING (s):	59.26	3.855	1.947	4.048	2.017	Very Poorly Sorted
SKEWNESS (Sk):	1.377	-0.353	0.353	-0.208	0.208	Fine Skewed
KURTOSIS (K):	4.465	2.053	2.053	0.779	0.779	Platykurtic

b

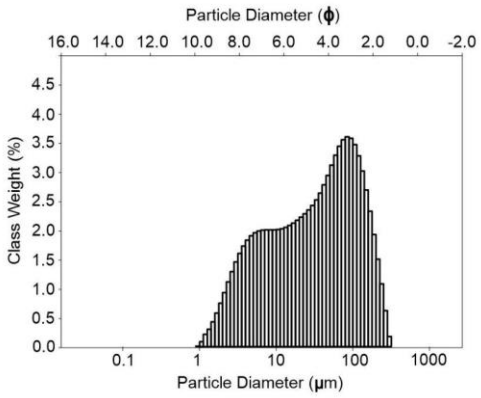

Figure S2. **a.** Grain-size characterization of the analysed volcanic ash layer obtained with the Grain Size Analysis Program GRADISTAT[23]. **b.** Grain-size distribution curve of the analysed tephra. Particle diameter is shown as both micrometres (µm) and phi (ϕ).

Chemical analyses indicate a homogeneous rhyolitic composition for glass and a scattered composition for biotite phenocrysts, which cover a large range in Mg/(Mg+Fe^{2+}_{tot}+Mn) and exhibit a total alkali content ranging from 1.75 to 1.90 apfu (atoms per formula unit), lower than the stoichiometric value of 2 apfu (Fig. S3).

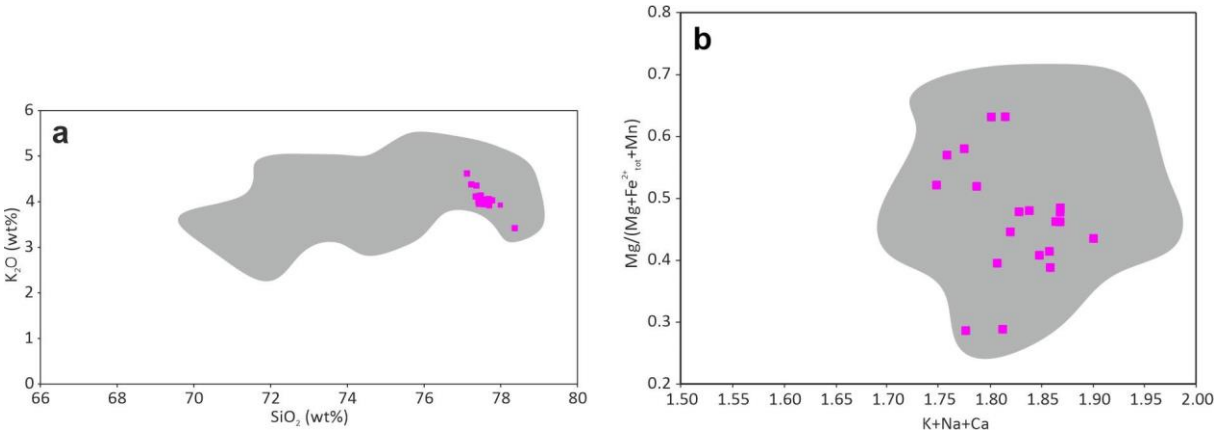

Figure S3. a. Volcanic glass K_2O vs SiO_2 diagram showing the glass composition of the analysed tephra. The grey field indicates the composition of the volcanic ash layers in the Eocene Paracas and Otuma formations. **b.** Biotite Mg/(Mg+Fe^{2+}_{tot}+Mn) v. K+Na+Ca diagram showing the biotite composition of the analysed tephra. The grey field indicates the composition of the volcanic ash layers in the Eocene Paracas and Otuma formations.

Even the compositional signatures of the analysed material are heterogeneous (Figs. S4,S5). This should be combined with the concentration data calculated from the irradiation-produced ^{39}Ar, ^{38}Ar, and ^{37}Ar: K = 6.64%, Cl = 1690 ppm, Ca = 1510 ppm. The K concentration is in the range of the variable EPMA spots on single grains, and is lower than the stoichiometric one. This suggests a diagenetic alteration during submarine burial as reported for marine tephra layers[24]. In order to quantify the alteration and qualitatively describe the authigenic phases, we refer to the EPMA spot analyses. However, these may not be entirely representative of the alteration, as they may not be perfectly comparable to the grains used for dating. It is observed that Na concentrations anti-correlate with K (Fig. S4a). This could be a genuine magmatic signature. However, the alkali site occupation is quite low, as mentioned above, which strongly suggests diagenetic alteration. The results of the alteration are displayed in Fig. S4b as a function of the Na/K ratio (taken as an alteration proxy, as it is likely to be modified by marine-derived interstitial waters after the tephra was sedimented). The Cl/K ratio (open circles) decreases as the alteration progresses; the main cluster corresponds to 0.10 < Na/K < 0.15, corresponding to Cl/K ratios between 0.015 and 0.020, as shown by all biotite heating steps except the first. In the same abscissa interval, the Ca/K ratio (filled triangles) ranges between 0 and 0.005. A possible correlation between Cl/K and Ca/K in the EPMA analyses is explored in Fig. S4c. In the Cl/K range between 0.015 and 0.020, typical of the present biotite, the Ca/K ratio is observed to increase up to 0.05, but without a clear negative correlation. This would be compatible with a biotite having a constant Cl/K ratio, in which some of the interlayer cation K is substituted by Ca. This hypothetical clintonite component would make up at most 5% of the biotite. Fig. S4c also shows a second, separate array: four EPMA points out of 20 have Cl/K ratios lower than biotite by up to a factor 3. Such low Cl/K ratios are more typical of feldspars, and could be diagnostic of diagenetic feldspar (adularia or albite) growth. This secondary origin is supported by the observation that the highest Na/K EPMA spots are those with the lowest Cl/K ratios, which in the step-heating also correspond to the lowest step ages.

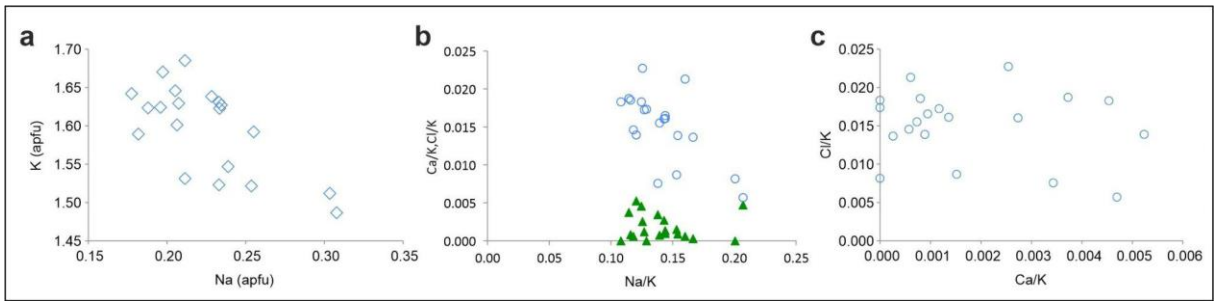

Figure S4. Chemical composition of the volcanic biotite crystals analysed by EPMA. **a**. K vs. Na correlation diagram of biotite crystals (apfu = atoms per formula unit). **b**. Ca/K (filled triangles) and Cl/K (open circles) vs. Na/K correlation diagram. Na/K varies by a factor 2 and is negatively correlated to Cl/K and (less well resolved) also to Ca/K. **c**. Cl/K vs. Ca/K diagram showing a lack of correspondence between low Cl/K (monitoring authigenic feldspar) and increased Ca, which suggests that up to 0.5% Ca are incorporated in the biotite interlayer.

It is conceivable that in a diagenetic environment dominated by calcite-saturated interstitial waters a two-step reaction might have occurred in addition to the secondary feldspar formation: biotite to talc; talc to Ca-rich (clintonitic) biotite. The alkali site depletion can reach up to 13% (Fig. S3b), whereas Ca incorporation is clearly subordinate by mass balance, of the order of 0.5-1% at most. However, since the desired precision is better than 1%, this reaction could bias the age estimate.

The common-denominator three-isotope correlation diagrams show no simple binary mixing. In general, the younger step ages correspond to higher Ca/K ratios, which is evidence of one or more Ca/K rich secondary mineral(s) (Fig. S5a). The Cl/K-age diagram shows no single trend, but sub-trends defined by contiguous steps can be recognized (FigS5b). In particular, the three steps having the lowest Ca/K ratio (steps 3-5) define a positive correlation between Cl/K and Ar*/K ratios. As a working hypothesis, one can propose the presence of three mineral phases: (a) relict, unreacted volcanic biotite; (b) diagenetic feldspar, expected to show the lowest Cl/K ratios; (c) diagenetic clintonite substitution. The trends could thus be explained in terms of a mixture of young secondary feldspar (whose age would best be approximated by step 10 with the lowest Cl/K ratio and a step age of 36.44 ± 0.07 Ma; here and in the following, uncertainties are given as 1 sigma) with primary, unreacted biotite. Unreacted biotite is best approximated by step 3, having a Cl/K signature furthest removed from that of step 10, and having an age of 36.77 ± 0.06 Ma (Fig. S5a and Supplementary Table S5). The four steps 6-9 have comparatively uniform Ca/K and Cl/K signatures and uniform ages, compatible with degassing of a biotite with a detectable secondary clintonite component.

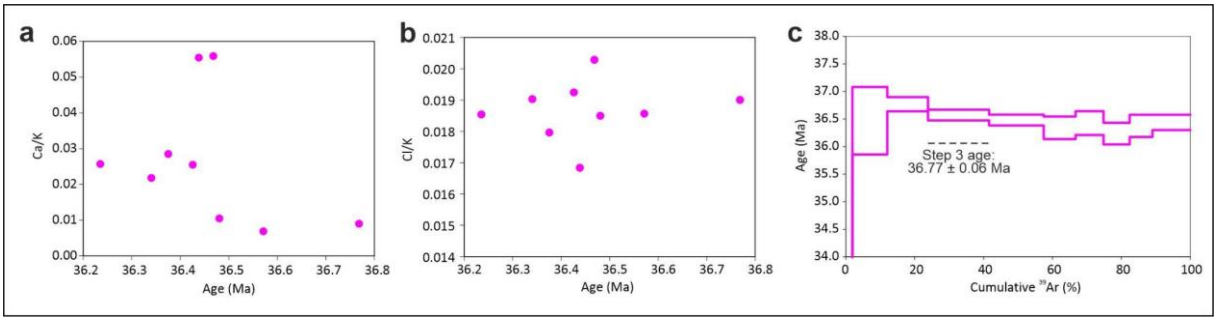

Figure S5. a. Ca/K vs. age diagram of the analysed tephra. Ca/K is calculated from the irradiation-produced $^{37}Ar/^{39}Ar$ ratio. **b**. Cl/K vs. age diagram of the analysed tephra. Cl/K is calculated from the irradiation-produced $^{38}Ar/^{39}Ar$ ratio. **c**. Age spectrum of the dated tephra. The filled rectangle highlights step 3, i.e., the step that better approximates the Ar release from the unreacted biotite.

Attempts to calculate an isochron from all steps, and specifically from the three Ca-poorest steps, fail to give an acceptably low dispersion (the lowest MSWD is 10.3), as calculated by the Isoplot program[25]. This is undoubtedly due to the lumped regression of non-cogenetic and non-contemporaneous mineral phases. The only low-dispersion alignment (MSWD= 0.94) is formed by the four steps assigned to the hypothetical "clintonitic biotite"; its isochron age is 36.33 ± 0.16 Ma, with an atmospheric initial Ar. It is therefore legitimate to calculate a weighted average age of steps 6-9, which gives 36.34 ± 0.05 Ma. This age is coincident, at the 1 sigma level, with that of the presumed diagenetic feldspar. We therefore propose this age to date the formation of the diagenetic minerals. In summary, the primary age of the tephra is proposed to be ≥ 36.8 ± 0.1 Ma; the secondary formation of diagenetic minerals occurred until approximately 36.3 Ma.

In this perspective, even the age spectrum can be useful: diagenesis was pervasive, as reflected by the plateau-like horizontal segment. The primary age is not very well preserved and is recorded by the oldest step, whose age discordance corresponds well with the discordant chemical (Ca/Cl/K) signature.

Types of skeletal mass estimations

Direct weighting. Extant mammal skeletal weights were taken from the literature: 1. terrestrial mammals' data are from the dataset of Prange et al.[26] (see exception for the Etruscan shrew below); 2. fully aquatic mammals' data are from Robineau & Buffrénil[27] and Domning & Buffrénil[28], to which was added the Wexford blue whale (NHMUK ZD.1892.3.1.1.: 2645 kg; Lorraine Cornish, pers. comm. 2022).

Large cetaceans. Average SM values for the blue whale (*Balaenoptera musculus*) and sperm whale (*Physeter macrocephalus*) were extrapolated from the SF (from Robineau & Buffrénil[27]) and the BM estimations (see below; Supplementary Table 6).

Sauropod estimations. SM was estimated for *Diplodocus* (CM84) based on the data of Larramendi et al.[29], multiplying skeletal elements' bone volume by bone density (Supplementary Table 7). Density of fresh compact and trabecular bone was adjusted, lowering them by 5% to exclude the free water content[30]. For largest sauropod estimate, *Argentinosaurus huinculensis*[31] (PVPH 1; known by a less complete skeleton than CM84), SM was extrapolated from *Diplodocus*' SF (using BM[31]; Supplementary Table 8). For *A. huinculensis*, this is hence a rough approximation (to be compared to the terrestrial mammals' scaling, see below), because it is likely that SF also scaled allometrically in sauropods.

Small extant amniotes. Whole skeleton volume was measured based on high-resolution CT data for the Etruscan shrew (*Suncus etruscus*; SMNS-Z-MAM-49066; scanned with a Bruker SkyScan1272 at a resolution of 0.0134 mm (images acquired with Control software 1.1.13 and reconstruction made with NRecon 1.7.1.6); deposited on MorphoSource (https://doi.org/10.17602/M2/M510260), the dwarf chameleon (*Brookesia nana*; UADBA-R/FGZC 3752; ark:/87602/m4/M101463; Glaw et al 2021; accessed on MorphoSource.org), and the Island least gecko (*Sphaerodactylus sputator*; ummz-herps-174801; ark:/87602/m4/M70974; accessed on MorphoSource.org). CT-scans were thresholded to measure the number of pixels occupied by bone tissue (measured with Fiji[32], ImageJ 1.52h[33], 'Threshold' routine using 'Stack histogram' option, then 'Histogram' routine), which was then multiplied by the resolution to the third power). Bone volume was then multiplied by the terrestrial mammal dry bone tissue density (see above; Supplementary Table 9).

Extinct sirenians. Whole skeleton volume was estimated based on surface models of the recently extinct (ca. 250 years) Steller's sea cow (*Hydrodamalis gigas*; NHMW-Zoo-MAMM 614, accessed on Sketchfab.com) and the Oligocene dugongid *Kaupitherium bronni* (SMNS-P-47736; built with the photogrammetry software Agisoft PhotoScan 1.21). Skeleton volume measurements (which entailed subtraction of non-skeletal elements) were acquired with MeshLab[34]. Whole skeleton volume was then multiplied by the overall skeletal density of the extant dugong (*Dugong dugon*). The latter was obtained using individual skeletal element densities[35] multiplied by the relative mass of the skeletal region (own measurement of SMNS-Z-MAM-1288; Supplementary Table 11). These data were augmented by the whole skull density (not assessed in Buffrénil & Schoevaert[35]). The whole skull density was estimated by assessing the bone mass (see compact bone density of the *D. dugong* above) and dividing it by the whole volume of the 'outer skull surface' (to 'mimic' surface models): a skull surface model made with CT-scan data (NHMUK 2005-51; Fiji/ImageJ[32,33], 'Threshold' routine using

'Stack histogram' option, then 'Histogram' routine, plugin '3D Viewer', 'Export surfaces' routine) and then the skull outer openings (e.g., foramen magnum) were closed (Meshlab, 'Screened Poisson Reconstruction' filter; Supplementary Table 10). For the largest sirenian individual, referred to the Plio-Pleistocene sea cow *Hydrodamalis cuestae* (LACM 25917[36]), known from fragmentary material, the estimations were made scaling up *Hydrodamalis gigas'* estimations based on body length (which should be seen as a rough estimate). The latter was estimated using the basicondylar skull length equation relying on combined *D. dugong* and *Trichechus manatus latirostris* (extant Florida manatee) data of Sarko et al[37]. (Supplementary Table 12).

***Prodeinotherium*.** The volume of the skeletal elements of the Miocene proboscidean *Prodeinotherium* (NHMW2000z0047/0001) was measured on a surface model (accessed on Sketchfab.com). This volume, to the exclusion of the long bones, was multiplied by the corresponding skeleton density of a terrestrial mammal (*Panthera leo;* Supplementary Table 16). The latter was taken from Buffrénil & Schoevaert[35] except for the whole skull, mandible, pelvis and foot values (not assessed therein; Supplementary Table 15). These three densities were assessed weighting the elements and measuring their volume based on surface models (Surface scanner: EinScan Pro HD, Shining 3D, EXScan Pro 3.7.0.3 software; skull and mandible: SMNS-Z-MAM-49240; pelvis and foot: SMNS-Z-MAM-2055; Supplementary Table 14). For the long bones' density (higher in graviportal taxa), we used that of the femur of the Pleistocene elephant *Palaeoloxodon antiquus* (based on the data of Boschian et al.[38]), following Larramendi[39] (Supplementary Table 13).

Largest terrestrial mammals on record. To place the Oligocene rhinoceros *Paraceratherium transouralicum* (AMNH 26168/75) and Asian Pleistocene straight-tusked elephant *Palaeoloxodon namadicus* (Sagauni II) in the analysis, we used their body mass estimate[39] and our extant-terrestrial-mammal regression (see Methods section of main text). The resulting estimates should be seen as very rough, as the body mass of both taxa largely exceeds the maximum value included in the regression.

Body mass estimations

Direct body mass (BM) measurements associated with the specimens were only available for terrestrial mammals (Prange et al[26], with the exception of the Etruscan shrew *Suncus etruscus*), small cetaceans (Buffrénil[40]), and manatees (Domning and Buffrénil[28]). The data of Prange et al. [26] were extended with new measurements to more evenly cover the mammalian range of body sizes (Supplementary Data 2): for most antelopes, the keratin sheath was weighted along with the skulls. The corresponding mass was subtracted using as a reference a 25.4 % ratio for the sheath mass to skull + sheath mass (measured on the antelope *Damaliscus lunatus* ZMH-MAM-0007916). The value of Prange et al.[26] for *Homo sapiens* departs greatly from those reported elsewhere (as already pointed out[29]), so it was replaced with the data of O'Flaherty[41]. In the same way, the values for the elephant from Prange et al.[26] were replaced by more reliable data[29]. For large cetaceans, we used the 'body length ~ BM' regressions of Lockyer[42], following Robineau and Buffrénil[27] (Supplementary Table 6). This concerns the specimens with weighted skeletons. Mean blue whale and sperm whale BM were taken from AnAge[43].

For sauropods, we have focused on the specimen with the most elaborate BM estimate, *Diplodocus* (CM 84[29]). The largest sauropod estimate, for *Argentinosaurus huinculensis*, comes from Campione & Evans[31]. For the latter, we have included minimum, intermediate, and maximum estimates.

For *Suncus etruscus* (SMNS-Z-MAM-49066), BM was taken from the species mean reported in AnAge[43]. For the small extant reptiles *Brookesia nana* (dwarf chameleon) and *Sphaerodactylus sputator* (island least gecko), the scanned specimens' BM was estimated from 'Snout-Vent Length (SVL) ~ BM' regressions for Chamaeleonidae and Gekkonidae, respectively[44]; SVL was taken from the original description for the former[45] and measured on a 3D rendering (made with Fiji/ImageJ[32,33]) with Meshlab[34] for the latter (Supplementary Table 9).

The BM of the extant *Dugong dugon* specimen SMNS-Z-MAM-1288 was estimated using the species' regression 'Condylobasal skull length (BSL) ~ BM' (Sarko et al 2010). We also used the regressions of Sarko et al (2010) to estimate the BM of the extinct sirenians *Kaupitherium bronni* (SMNS-P-47736), *Hydrodamalis gigas* (NHMW-Zoo-MAMM 614), and *Hydrodamalis cuestae* (LACM 25917): minimum, intermediate, and maximum estimates are based on BSL equations that use *Dugong dugon*, *Trichechus manatus latirostris*, and the combination of both taxa (Supplementary Table 12). Because of the rather strong pachyostosis affecting *K. bronni*, we expect that the skull-based body mass estimation will yield underestimates.

For the extinct terrestrial mammals *Prodeinotherium*, *Paraceratherium transouralicum*, and *Palaeoloxodon namadicus*, BMs were directly taken from published estimates (Larramendi 2015).

Bone histology of *Perucetus colossus*

To produce the rib thin-sections, first a half-moon shaped thick-section had to be extracted at mid-diaphysis (Fig. S6a,b) with a circular saw equipped with a diamond blade. This thick-section was then processed in three separate chunks to obtain the thin-sections.

For the vertebrae, core drills were extracted at representative locations (Fig. S6c,d) following the methodology of Stein and Sander[46]. Several vertebrae were sampled, due to their preservation: Th-a, centrum posteroanterior drill; L-c, neural spine drill; L-e, centrum dorsoventral drill and transverse process.

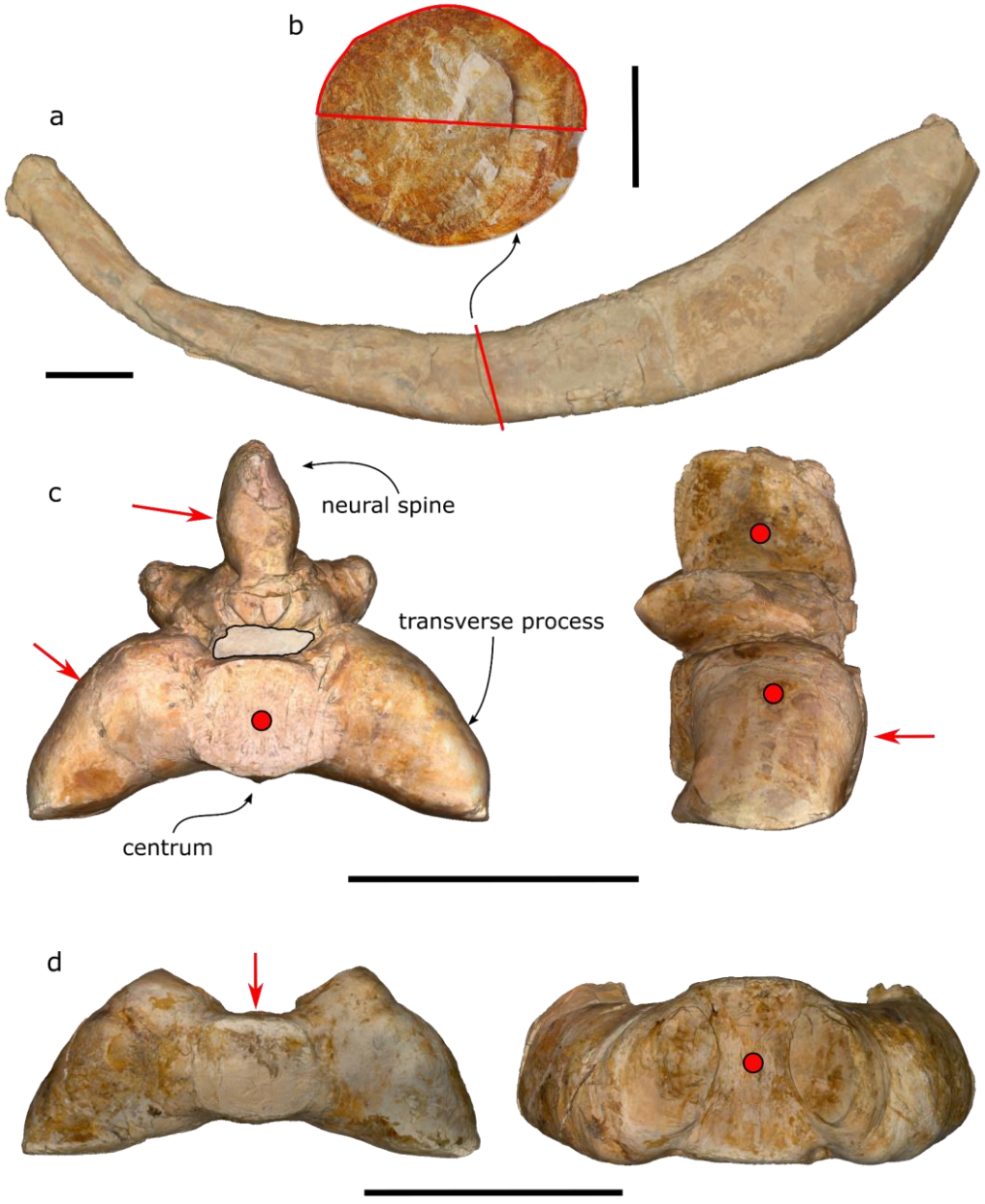

Figure S6. Histological sampling of the holotype of *Perucetus colossus* (MUSM 3248). a. whole rib (anterior view, 3D surface model with texture) with sampled location. **b.** half cross-section used for thin-sections. **c.** Complete lumbar vertebra in posterior (left), left lateral (right) views**. d.** Lumbar

vertebra missing neural arch in anterior (left) and dorsal (right) views. Sites of core samples are indicated with red arrows and circles. Scale bars, 10 cm (a), 5 cm (b), and 50 cm (c,d).

Perucetus colossus skeletal and body mass estimations

Skeleton length and volume. As outlined in the Methods section (main text), we have used Cy*nthiacetus peruvianus*' holotype[47] (MNHN.F.PRU10) as a basis for the estimation of *P. colossus*' whole skeleton. We first scaled up *C. peruvianus*' skeleton. Ten vertebrae of *P. colossus* are complete enough to be used for this process, among which two thoracic (T) and eight lumbar (L) vertebrae. Because the precise location of these vertebrae is unknown, we have randomly drawn (10 000 times, *sample* function, base of R) the elements of *C. peruvianus*' holotype that could match (based on overall morphology), i.e., two among T17-20 and eight among L1-20 (R script, https://github.com/eliamson/ColossalCode). We then took the mean values of the centra' mediolateral width (anterior side), dorsoventral height (anterior side), and anteroposterior length, and divided it by the corresponding measurements on *P. colossus*' measurements to obtain ratios (Supplementary Table 17) to be used to stretch *C. peruvianus*' vertebral column in the three corresponding directions (Blender 3.0.1[48]; scaling along X, Y, Z; Fig. S7a,b).

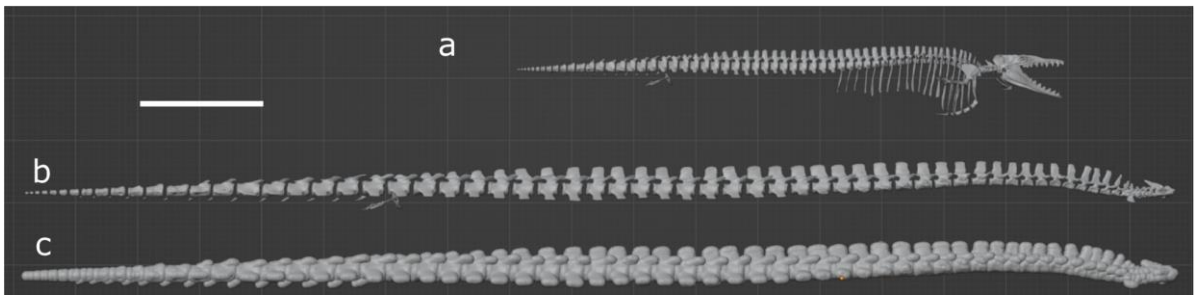

Figure S7. Scaling up and dilating the vertebral column of Cy*nthiacetus peruvianus*' holotype (MNHN.F.PRU10) to match the volume of the recovered bones of *Perucetus colossus*. a. Unmodified 3D model of C. *peruvianus*' holotype. **b.** Scaled-up model. **c.** scaled-up and dilated model. Scale bar = 2 m.

For the ribcage, the same approach was not used, because of the clearly different proportions between the scaled up *C. peruvianus* vertebral column and the measured rib of *P. colossus* (which entails a relatively much larger rib cage for the latter). We hence have scaled up the rib cage of *C. peruvianus* according to two possibilities (both using the chord , i.e., straight length from proximal to distal ends): a conservative scaling, assuming that the recovered rib corresponds to *C. peruvianus*' anterior-most rib with simple proximal end morphology (R17; chord = 47 cm); and assuming that the rib corresponds to *C. peruvianus*' posterior-most rib (R20; chord = 39 cm). The corresponding ratios (2.34 and 2.82, respectively) were used to scale the ribs in all directions (Fig. S8b, d). For the other skeletal elements (skull and mandible, girdles, and limbs), we simply scaled them using the width and height ratio obtained for the vertebral column (there is no reason to assume an anteroposterior lengthening of these bones, contrary to the vertebrae, which are clearly more elongate in *P. colossus*' than in *C. peruvianus*. This scaled-up skeleton is 20.0 m long.

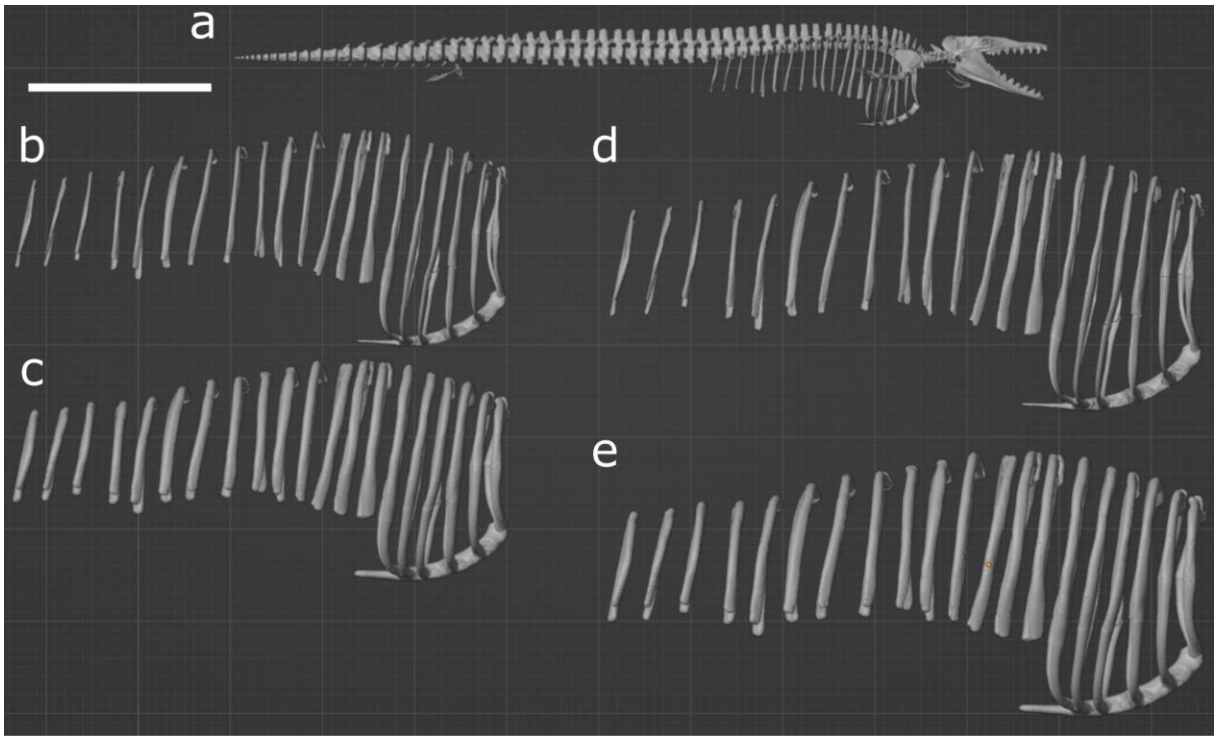

Figure S8. Scaling up and dilating the ribcage of Cy*nthiacetus peruvianus*' holotype (MNHN.F.PRU10) to match the volume of the recovered rib of *Perucetus colossus*. **a.** Unmodified 3D model of C. *peruvianus*' holotype. **b.** Scaled-up model, ratio = 2.34. **c.** same model, dilated. **d.** Scaled-up model, ratio = 2.82. **e.** same model, dilated. Smallest square side = 10 cm.

Because of the strong pachyostosis characterising *P. colossus,* the volumes of virtual bones resulting from the scaling up *C. peruvianus* were still much lower than those of the new taxon. As for the procedure to scale up the vertebrae, we measured the volumes of the complete enough vertebrae of *P. colossus*, i.e., one thoracic and four lumbar vertebrae, randomly drew the corresponding bones of *C. peruvianus* (among T17-20 and L1-17), measured the volumes on the scaled-up model, and obtained a mean value for the five vertebrae. The ratio between the latter value and the added volumes of *P. colossus'* complete enough vertebrae (4.58) was then used to estimate the latter species' total vertebral column volume (2.72 m^3). Dilating the scaled-up vertebral column (moving the faces along the normals; Blender, *Fatten* function) of 5.85 cm yields this volume; the resulting model will be referred to as scaled-up and dilated (Supplementary Table 18; Fig. S7c). Similarly, for the ribcage, we dilated the pair of 17th and 20th ribs of the scaled up models (see above) to match the volume of *P. colossus'* rib, which respectively required a displacement of 1.05 and 2.39 cm (Fig. S8c, e). We conservatively did not dilate the other skeletal elements.

With this methodology relying on *C. peruvianus* as a basis, we made additional estimates editing the scaled-up, dilated model to match the skeletal composition of other basilosaurids. A *Basilosaurus isis* version was obtained removing two thoracic segments (thoracic vertebrae and ribs 12-13, median of the series based on rib dimensions) and adding two lumbar vertebrae (L8-9, median of series) (based on Gingerich et al.[49]). A *Dorudon atrox* version was done removing three thoracic segments (T12-14) and adding three lumbar vertebrae (L7-9) (based on Uhen[50]). The resulting scaled-up (non-dilated) skeletons are both 20.1 m long. Complete pachycetine vertebral columns are hitherto unknown[51]; but their vertebral count was likely lower than that of other basilosaurid. A conservative counts of 12 thoracic (as in *Pachycetus wardii*[52]; removing T3-4 and T11-16 and the corresponding ribs, which form the median thoracic segments based on rib dimensions) and 15 lumbar vertebrae (minimum count documented in the family[47]; removing L8-9, median of series). See all estimated volumes in

Supplementary Table 18). Removing these elements from the scaled-up (non-dilated) skeleton of *C peruvianus* (see above), a conservative skeletal length of 17.0 m is obtained.

Skeleton mass. The minimum and maximum volumes obtained above were multiplied by each skeletal element density. For the vertebrae and ribcage, the density was obtained by multiplying the global compactness of the rib and that of vertebral parts (centrum, neural arch, and transverse processes) by the mean dry bone tissue density of *Delphinus delphis* (see Methods section, main text). The global compactness of the rib (0.995) corresponds to an observation at mid-diaphysis; observations of break surfaces confirm that a similar microanatomy (i.e., highly compact) characterises the rest of the rib, too. The global compactness of the vertebrae was assessed based on core drills made in the centrum (a dorsoventral one at the anteroposterior half the centrum and a posteroanterior one made in the middle of the posterior side of the centrum), neural arch (sampled at the dorsoventral half of the neural spine, lateral side), and transverse process (roughly at its mediolateral half, dorsal side) of lumbar vertebrae (Fig. S6). While the core drills obtained for the neural spine and transverse process (Extended Data Fig. 7a2,3, respectively) do not reach the middle of the elements, observation of break surfaces confirms that the microanatomy is very consistent across their whole depth (i.e., there is no free or even spongious medulla, the processes are compact throughout; Fig. S11). The compactness values measured for the corresponding sections (i.e., 0.983 and 0.838. respectively) were hence associated with these vertebral parts. The dorsoventral core drill of the centrum (Extended Data Fig. 7a1) shows a clear gradient of compactness from the periosteal surface to the centre (Extended Data Fig. 7). To extrapolate the surface sampled by the core to the whole centrum's cross-section, we measured bone compactness in ten areas of equal height along the core drill with an ImageJ macro (which was enough to capture the observed variation; ImageJ macro, https://github.com/eliamson/ColossalCode). The centrum's cross-section was approximated as an ellipse to estimate the surface occupied by each successive, concentric layer (R script, https://github.com/eliamson/ColossalCode; Supplementary Table 19). Given that the dorsoventral radius (half of the dorsoventral height) of the sampled centrum slightly exceeds the total length of the sampled core (77.4 mm), an eleventh zone was added as the innermost one with the corresponding height (27.6mm). The compactness of the deeper sampled area (which reached the spongious core of the centrum) was ascribed to the 11th area. The mediolateral diameter of the sampled centrum (253 mm) was used to complete the calculation of each area's surface. Each surface was multiplied by the centrum's anteroposterior length minus the length of the posteroanterior core drill times two, which was made to assess the compactness of the anterior and posterior ends of the centrum. Each volume was finally multiplied by the corresponding compactness measurement. The same procedure was followed to assess the bone volume of the centrum's anterior and posterior ends (based on a posteroanterior core drill made in the centre of the posterior face of the centrum, Fig. S12), except that it was not necessary to add an eleventh zone. An overall compactness of 0.783 was obtained for the centrum. Given that some parts of the inner cortex and spongiosa might have been taphonomically eroded (see Supplementary Discussion), this should most likely be seen as an underestimation (which affects the downstream estimates, including the final body mass).

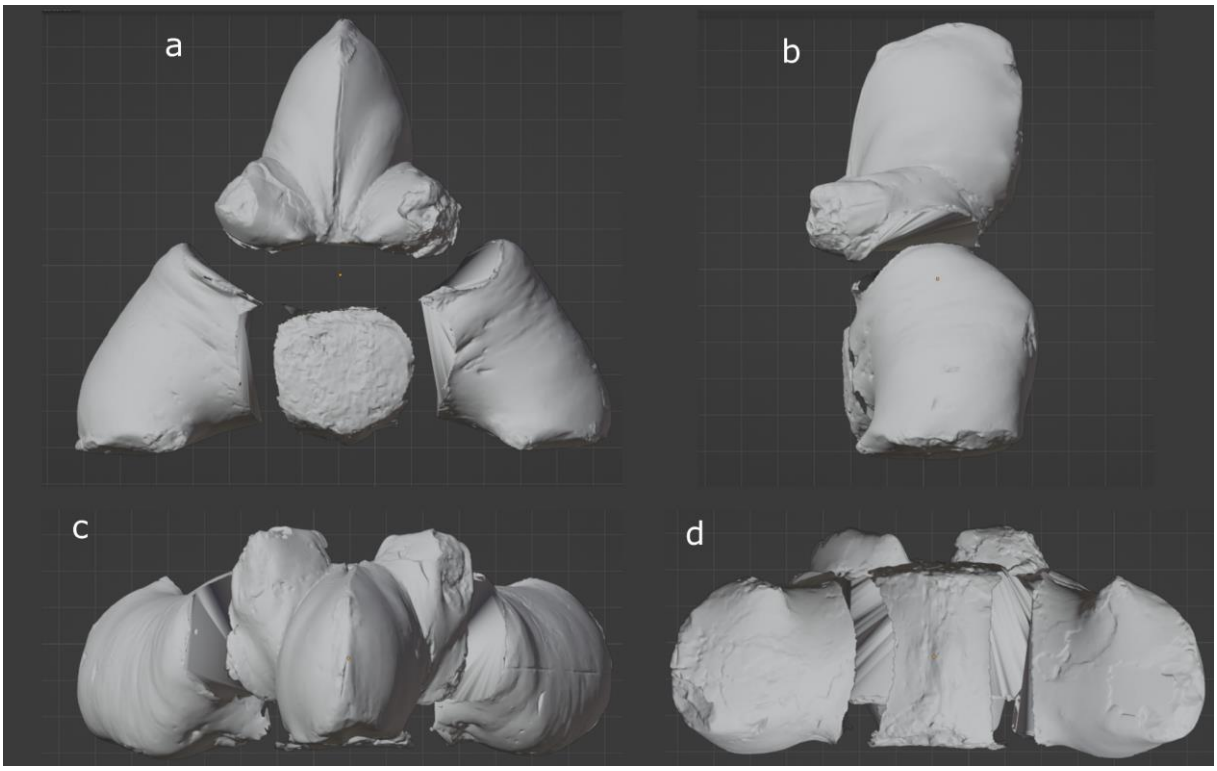

Figure S9. Relative volumes of vertebral parts. The relative volumes of *P. colossus* vertebral parts were measured splitting the 3D models into closed objects representing the centrum, neural arch, and transverse processes. **a.** Anterior view. **b.** Left lateral view. **c**. dorsal view. **d.** ventral view.

To estimate the relative proportions of centrum, neural arch, and transverse processes for the whole vertebral column, we used as a base the holotype of *Cynthiacetus peruvianus* (MNHN.F.PRU10), as for the overall volume estimation. Haemal arches were not considered as they are not known in *P. colossus* and represent but a minute percentage of the skeleton's volume in other basilosaurids. Parts of each vertebra were isolated for their respective volumes to be measured (in Blender 3.0.1[48]; Supplementary Data 4). In total the vertebral column of this specimen is made of 79% of centrum, 14% of neural arch, and 8% of transverse processes. As above, 10 000 random draws were made to select vertebrae in the lumbar regions of *C. peruvianus* corresponding to those of *P. colossus* for which the same volume measurements were made (Fig. S9; Supplementary Table 19; R code at https://github.com/eliamson/ColossalCode; see also Supplementary Discussion). Here we used the vertebral parts' proportions of four of the complete enough lumbar vertebra of *P. colossus* (one thoracic is complete enough but was excluded from this estimation, because of its widely different proportions when compared to the thoracics of *C. peruvianus*). *P. colossus*' vertebrae are made on average and in terms of volume of 19% of centrum, 29% of neural arch, and 54% of transverse processes. These proportions are, for the holotype of *Cynthiacetus peruvianus*, 4.2 times smaller for the centrum, 2.2 times larger for the neural arch, and 4.8 times larger for the transverse processes. Extended to the whole vertebral column, and with the compactness measurements described above, it can be estimated that the overall global compactness for *P. colossus*' vertebral column was 0.877.

For the skull and mandible (which represent less than 3% of the skeleton in volume), we multiplied the density that was obtained using a *Delphinus delphis* specimen, which was weighted and surface-scanned (EinScan Pro HD, Shining 3D, EXScan Pro 3.7.0.3 software; Supplementary Table 21).

For the limbs (<1% of the whole skeleton volume), we used the *Delphinus delphis* data of Buffrénil et al. (1986). This is probably an underestimation, as in *Cynthiacetus* (who does not show marked pachyosteosclerosis[53]), the humeral cortex at mid-diaphysis is slightly thicker than in extant cetaceans. The skeletal mass corresponding to the different estimations are presented in the Supplementary Table 22.

Supplementary Discussion

Bone histology of *Perucetus colossus*

Ribs and vertebrae

The periosteal-most layer (ca. 50 µm or less) is missing for a large portion of the rib section. Nevertheless, when present, an accumulation of parallel-fibered tissue is visible (Fig. S10a). This likely indicates the onset of the external fundamental system deposition, which in turn suggests that the animal was approaching skeletal maturity. Growth marks (annuli) are not conspicuous; only interruptions in the convoluted network of osteons indicate a change in the pattern of cortical apposition (Fig. S10b). The specimen is also often broken along the curvature of the annuli (Fig. 3a, main text). Similar growth marks were observed macroscopically on the ventral surface of vertebral pedicles (on broken-off neural arches; Fig. S11a), suggesting that a strong cortical drift directed laterally was also involved during the growth of the neural arch of the vertebrae. On broken-off transverse processes, similar growth marks are also present, but rather involving a cortical drift in the dorsal direction (Fig. S10b). A similar pattern of "step fractures" has been described for the vertebrae of the basilosaurids *Eocetus schweinfurthi* and *Pachycetus wardii*[54]. For both the rib and vertebral processes of *P. colossus*, the thickness of the growth zones (between the growth marks) is not conspicuously decreasing proceeding towards the ontogenetically older side of the bone, suggesting that the individual did not experience a strong overall reduction of growth rate during its ontogeny. As for the type of histological tissue (highly vascularised woven-parallel complex) making virtually the whole bone (see main text), this agrees with the condition described in *Basilosaurus*, which involves rapid periosteal accretion until an advanced ontogenetic stage[55]. Most of the osteons composing the woven-parallel complex observed in *P. colossus* are mature (with a small lumen), while the opposite is true for *Basilosaurus.* In that regard, *P. colossus* is reminiscent of the highly compact rostrum of the extinct beaked whale *Aporotus recurvirostris*[56]. This histology has been interpreted as indicative of the lack of bone resorption (which usually creates the spongy region of bones). In the dorudontine *Zygorhiza*, another bone histology and growth pattern is described: the deposition of peripheral lamellar zonal tissue suggests a slower growth during late ontogeny[55]. As in *Basilosaurus* and *Zygorhiza*, very few traces of remodelling are visible. In *P. colossus*, we only identified secondary deposition on resorption surfaces in the region of the rib section with larger vacuities, most likely corresponding to a large vascular canal (Fig. S10c-f). This vascular canal, which reaches the cross-sectional plane on three closely located places (Fig. S10c,d), is the only sizable porosity on the whole section. *P. colossus* differs from both *Basilosaurus* and *Zygorhiza* in lacking calcified cartilage. In the latter taxa, it is found in the medullary region of the rib, so the lack of calcified cartilage in *P. colossus* could be explained by the strong cortical drift that results in the loss of the initial medullary region.

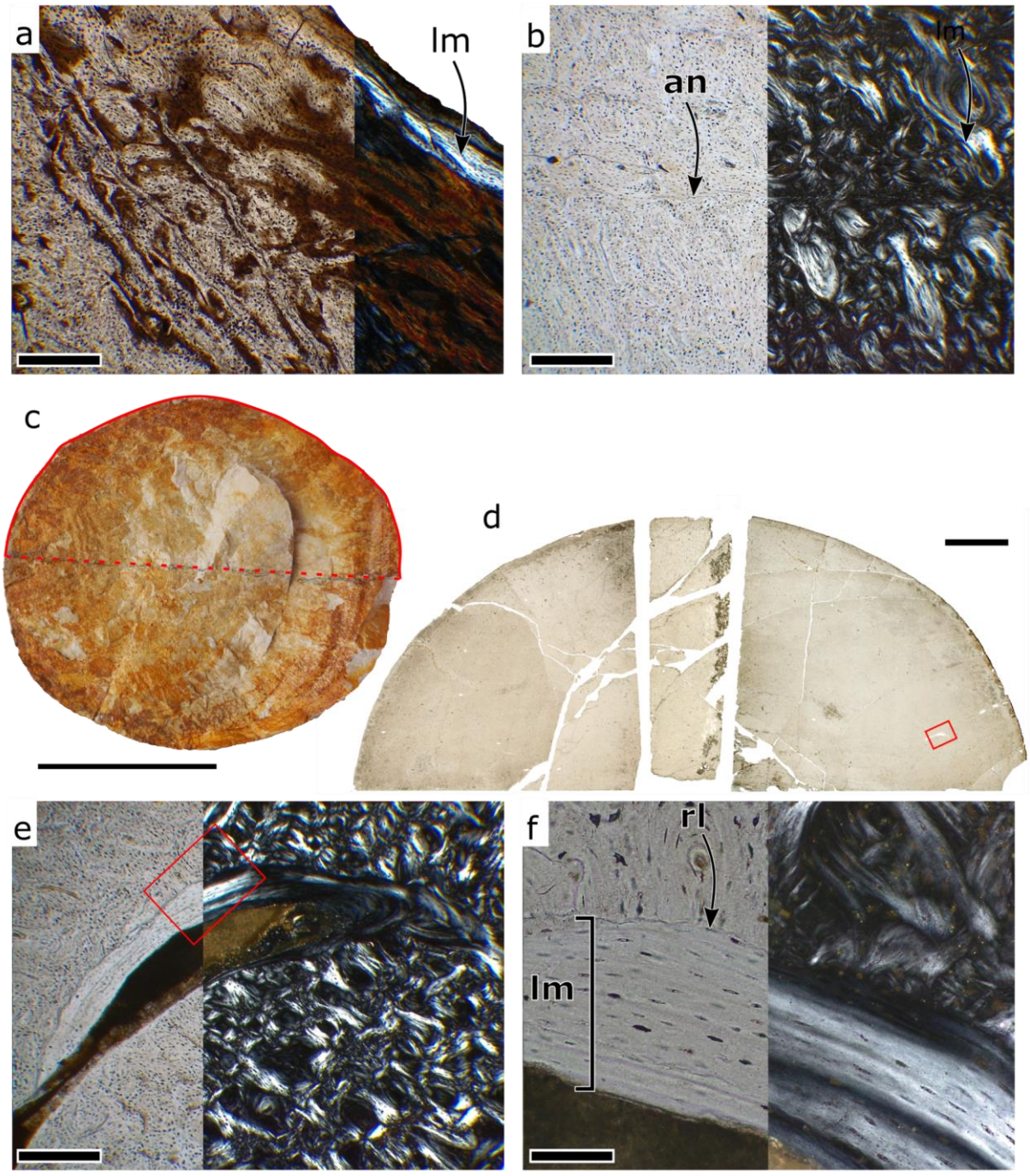

Fig. S10 Histological features of a rib of *Perucetus colossus* MUSM 3248, holotype. a. Periosteal region with lamellar bone suggesting the onset of the external fundamental system. **b.** Growth mark (annulus) in the middle of the cortex. **c.** rib surface break, roughly where the cross-section was made. **d.** half rib cross-section. **e.** Vascular canal lined with lamellar bone. **f.** Detail of **e**, showing the scalloped reversion line and lamellar bone. For all cross-sections except the overview (**c**, which is under natural light), the left part is under natural light and the right part under cross-polarized light. Red shapes in **c**-**e** indicate the zones shown in **d**-**f**, respectively. Scale bars, 500 µm (a, b, d), 10 cm (c), 1 cm (d), 100 µm (f). Abbreviations: an, annulus; lm, lamellar bone; rl, resorption line.

Bone microanatomy of *Perucetus colossus*

Vertebrae

In *P. colossus*, data from core drills and the observations of break surfaces suggest that the neural arch and transverse processes were mostly devoid of major porosity (Extended Data Fig. 7a2,3; Fig. S11). The core drill of the transverse process, however, shows a less compact structure (Extended Data Fig. 7a3). This reflects the fact that the woven-parallel complex composing the bone tissue is not as tight as in the other sections, with some space between the primary osteons.

The centrum does comprise a core of spongy bone, but most of its thickness is made out of compact tissue (Extended Data Fig. 7a1). The trabeculae in the centrum's core are actually very thin, the global compactness in the innermost section of the core is only 0.37. However, parts of some thin-sections seem to have been subject to some dissolution during taphonomy, suggesting that the existing porosity might have been artificially enlarged. The global compactness values for the centrum core drills might hence be underestimated. The centrum's epiphysis (sampled in the centre of the posterior face) is rather compact, but the bone directly internal is spongy (Fig. S12), as commonly found in the sub-epiphyseal region internal to unfused epiphyses.

Fig. S11. Break surfaces of the vertebrae of *Perucetus colossus* MUSM 3248, holotype. a. Peduncle of a lumbar vertebra in ventral view. **b**. Spinous process in posterior view (see Extended Data Fig. 2g-l). **c**. Transverse process (roughly at mid-length) in medial view. Scale bars = 5 cm.

Based on the observations of break surfaces, the apophyses of other basilosaurids always retain a spongy core: this was observed in the spinous process of *Pachycetus* NMNH-P OF-2096[57], the pedicle and transverse process of *Masracetus markgrafi* (SMNS 11414), and the spinous and transverse processes of *Eocetus schweinfurthi* (SMNS 10934). A thick cortex surrounding trabecular bone has also

been used to generally describe the microanatomy of vertebrae (and ribs) in *Eocetus schweinfurthi* and *Pachycetus wardii*[54]. In other basilosaurids, the centrum is also always mostly filled with loose spongy bone (this is the condition present in virtually all other mammals), even though a more compact structure due to local thickening of the cortex is described in pachycetines[51] and *Basilosaurus*[53]. An osteosclerotic condition for vertebral centra is quite uncommon. To the best of our knowledge, among mammals it is only clearly documented in the Miocene phocid *Nanophoca vitulinoides*, where it seems to involve infilling of the intertrabecular space[58] (other taxa also display locally a thicker cortex[59]). Pachyostotic vertebrae are also very uncommon among mammals, this being only clearly expressed in some sirenians and members of the Miocene Paratethys fauna that underwent a hypersaline event (i.e., the ?platanistid *Pachyacanthus*[60] and the phocid *Pachyphoca*[61]). In *Pachyacanthus*, a CT-scan of a lumbar vertebra (see Dewaele et al., 2021: Fig. 2A) also reveals that strong osteosclerosis affects the whole skeletal element (pers. obs.). While microanatomical data are not available for *Pachyphoca*, it is most likely that its vertebrae were (at least to some extent) displaying a more compact structure, too (given that pachyostosis is almost always associated with osteosclerosis, the exception being the Eocene sirenian *Pezosiren portelli*[62]). A few long-bodied reptiles also have pachyosteosclerotic vertebrae[59]. Global compactness values of *P. colossus* vertebral parts are indicative of the fact that the whole vertebra is affected by osteosclerosis (Supplementary Table 2). Comparisons with other cetaceans and sirenians confirm that greater amounts of porosity are usually found in the vertebral centrum and apophyses.

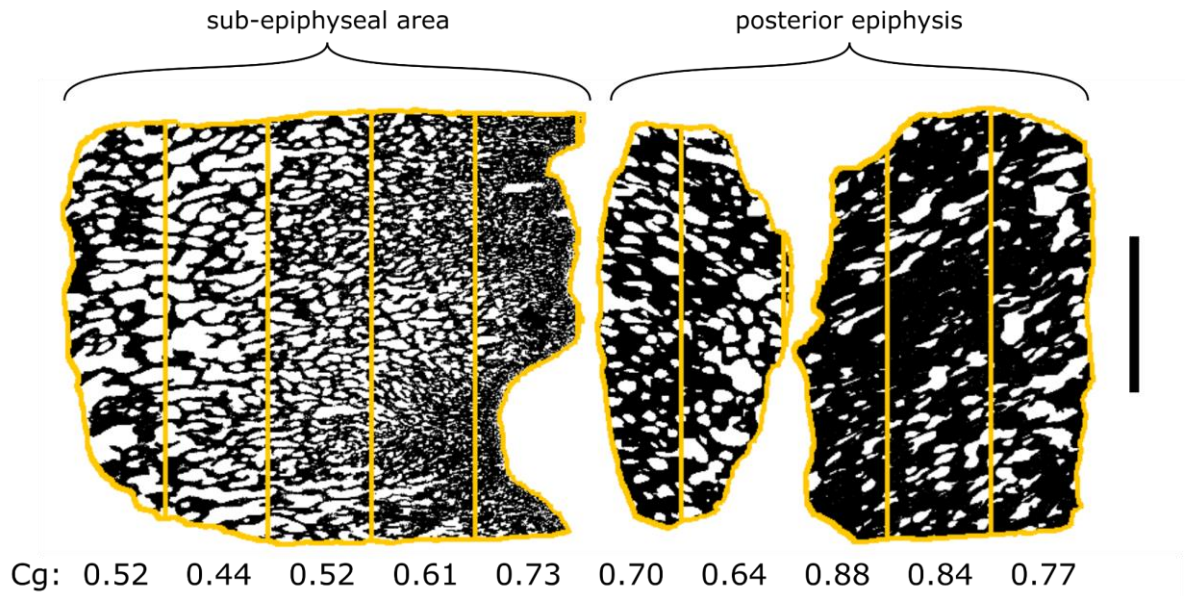

Fig. S12. Microanatomy of the posteroanterior core drill of a vertebra (Th-a) of *Perucetus colossus* MUSM 3248, holotype. Binarized sections (black = bone), exterior (posterior direction) towards right (see core drill location in Fig. S6c). The global compactness (Cg) was measured in ten areas (orange outlines) to assess overall centrum compactness (see above). Scale bar = 5 mm.

Several foramina and radial sulci pierce the anterior and posterior surface of the transverse processes near the dorsolateral margin of the vertebral centra and smaller pits are sometimes visible on the ventral surface of the centra of *P. colossus*. Such vascular openings and grooves, already observed in other basilosaurids[51,54], could be related to pachyostosis.

Ribs

The recovered ribs of *P. colossus* are all pachyostotic. Given the thin-section made for one rib, and the generalised osteosclerotic condition that otherwise affects all sampled locations, it is most likely that the whole rib cage of *P. colossus* was pachyosteosclerotic. This is also suggested by the fact that in basilosaurids with a weaker degree of pachyostosis, such as *Antaecetus aithai* for instance, the pachyostosis more strongly affects the anterior-middle of the rib series[51]. Pachyosteosclerotic ribs are found in multiple clades, for instance in sirenians and mesosaurs (in addition to some other basilosaurids[59]). While the global compactness value associated with the thin-section of *P. colossus* is extreme (0.995), similar values (denoting the absence of virtually any large porosity) are found in the ribs of other strongly osteosclerotic mammals (Supplementary Table 2).

Supplementary References

1. Hampel, A., Kukowski, N., Bialas, J., Huebscher, C. & Heinbockel, R. Ridge subduction at an erosive margin: The collision zone of the Nazca Ridge in southern Peru. *J. Geophys. Res. Solid Earth* **109**, (2004).

2. Pilger, R. H. Plate reconstructions, aseismic ridges, and low-angle subduction beneath the Andes. *Geol. Soc. Am. Bull.* **92**, 448–456 (1981).

3. Hsu, J. T. Quaternary uplift of the peruvian coast related to the subduction of the Nazca Ridge: 13.5 to 15.6 degrees south latitude. *Quat. Int.* **15**–**16**, 87–97 (1992).

4. Macharé, J. & Ortlieb, L. Plio-Quaternary vertical motions and the subduction of the Nazca Ridge, central coast of Peru. *Tectonophysics* **205**, 97–108 (1992).

5. Dunbar, R. B., Marty, R. C. & Baker, P. A. Cenozoic marine sedimentation in the Sechura and Pisco basins, Peru. *Palaeogeogr. Palaeoclimatol. Palaeoecol.* **77**, 235–261 (1990).

6. DeVries, T. J. Oligocene deposition and Cenozoic sequence boundaries in the Pisco basin (Peru). *J. South Am. Earth Sci.* **11**, 217–231 (1998).

7. DeVries, T. J., Urbina, M. & Jud, N. A. The Eocene-Oligocene Otuma depositional sequence (East Pisco Basin, Peru): paleogeographic and paleoceanographic implications of new data. B. Soc. Geol. Perú 112, 14–38 (2017). *Boletín la Soc. Geológica del Perú* **112**, 14–38 (2017).

8. Di Celma, C. *et al.* Towards deciphering the Cenozoic evolution of the East Pisco Basin (southern Peru). *J. Maps* **18**, 397–412 (2022).

9. Di Celma, C. *et al.* Sequence stratigraphy and paleontology of the Upper Miocene Pisco Formation along the western side of the lower Ica valley (Ica desert, Peru). *Riv. Ital. di Paleontol. e Stratigr.* **123**, 255–273 (2017).

10. Di Celma, C. *et al.* Intraformational unconformities as a record of late miocene eustatic falls of sea level in the pisco formation (Southern Peru). *J. Maps* **14**, 607–619 (2018).

11. Dunbar, R. B., Marty, R. C. & Baker, P. a. Cenozoic marine sedimentation in the Sechura and Pisco basins, Peru. *Palaeogeogr. Palaeoclimatol. Palaeoecol.* **77**, 235–261 (1990).

12. León, W., Aleman, A., Rosell, W., Torres, V. & De La Cruz, O. Estratigrafía, Sedimentología y Evolución Tctónica de la Cuenca Pisco Oriental. *Ingemet* 1–154 (2008).

13. DeVries, T. J. Eocene stratigraphy and depositional history near Puerto Caballas (East Pisco Basin, Peru). *Boletín la Soc. Geológica del Perú* **112**, 39–52 (2017).

14. Uhen, M. D., Pyenson, N. D., Devries, T. J., Urbina, M. & Renne, P. R. New middle Eocene

whales from the Pisco Basin of Peru. *J. Paleontol.* **85**, 955–969 (2011).

15. Coletti, G. *et al.* Biostratigraphic, evolutionary, and paleoenvironmental significance of the southernmost lepidocyclinids of the Pacific coast of South America (East Pisco Basin, southern Peru). *J. South Am. Earth Sci.* **96**, 102372 (2019).

16. Malinverno, E. *et al.* (Bio)stratigraphic overview and paleoclimatic-paleoceanographic implications of the middle-upper Eocene deposits from the Ica River Valley (East Pisco Basin, Peru). *Palaeogeogr. Palaeoclimatol. Palaeoecol.* **578**, 110567 (2021).

17. Collareta, A. *et al.* A rhinopristiform sawfish (genus *Pristis*) from the middle Eocene (Lutetian) of southern Peru and its regional implications. *Carnets de géologie* **20**, 91–105 (2020).

18. DeVries, T. J. *et al.* The Miocene stratigraphy of the Laberinto area (Río Ica Valley) and its bearing on the geological history of the East Pisco Basin (south-central Peru). *J. South Am. Earth Sci.* **111**, 103458 (2021).

19. Muñiz, F., Esperante, R. & Poma, O. La Icnoespecie Gyrolithes Vidali Mayoral 1986 En El Mioceno Superior De La Formación Pisco (Ica, Perú): Implicaciones Paleoambientales. *XXVII Jornadas la Soc. Española Paleontol.* 263–267 (2011).

20. Lowe, D. J. Tephrochronology and its application: A review. *Quat. Geochronol.* **6**, 107–153 (2011).

21. Griggs, A. J., Davies, S. M., Abbott, P. M., Rasmussen, T. L. & Palmer, A. P. Optimising the use of marine tephrochronology in the North Atlantic: a detailed investigation of the Faroe Marine Ash Zones II, III and IV. *Quat. Sci. Rev.* **106**, 122–139 (2014).

22. Tada, R. *et al.* Site U1425. in *In Proceedings of the Integrated Ocean Drilling Program* (eds. Tada, R., Murray, R. W., Alvarez Zarikian, C. and the Expedition 346 Scientists' addresses) 346 (2015). doi:10.2204/iodp.proc.346.106.2015.

23. Blott, S. J. & Pye, K. GRADISTAT: a grain size distribution and statistics package for the analysis of unconsolidated sediments. *Earth Surf. Process. Landforms* **26**, 1237–1248 (2001).

24. Villa, I. M. & Bosio, G. "Excess Ar" by laboratory alteration of biotite. *Geology* **51**, 121–125 (2023).

25. Ludwig, K. R. User's manual for Isoplot/Ex 3.7 and 4.15: a geochronological toolkit for Microsoft Excel. *Berkeley Geochronol. Cent. Spec. Publ.* **4**, 1–70 (2008).

26. Prange, H. D., Anderson, J. F. & Rahn, H. Scaling of skeletal mass to body mass in birds and mammals. *Am. Nat.* **113**, 103–122 (1979).

27. Robineau, D. & Buffrénil, V. de. Nouvelles données sur la masse du squelette chez les grands cétacés (Mammalia, Cetacea). *Can. J. Zool.* **71**, 828–834 (1993).

28. Domning, D. P. & Buffrénil, V. de. Hydrostasis in the Sirenia: quantitative data and functional interpretations. *Mar. Mammal Sci.* **7**, 331–368 (1991).

29. Larramendi, A., Paul, G. S. & Hsu, S. A review and reappraisal of the specific gravities of present and past multicellular organisms, with an emphasis on tetrapods. *Anat. Rec.* **304**, 1833–1888 (2021).

30. Surowiec, R. K., Allen, M. R. & Wallace, J. M. Bone hydration: How we can evaluate it, what can it tell us, and is it an effective therapeutic target? *Bone Reports* **16**, 101161 (2022).

31. Campione, N. E. & Evans, D. C. The accuracy and precision of body mass estimation in non-avian dinosaurs. *Biol. Rev.* **95**, 1759–1797 (2020).

32. Schindelin, J. *et al.* Fiji: an open-source platform for biological-image analysis. *Nat. Methods* **9**, 676–682 (2012).

33. Schneider, C. A., Rasband, W. S. & Eliceiri, K. W. NIH Image to ImageJ: 25 years of image analysis. *Nat. Methods* **9**, 671–675 (2012).

34. Cignoni, P. *et al.* MeshLab: an Open-Source Mesh Processing Tool. in *Eurographics Italian Chapter Conference* (eds. Scarano, V., Chiara, R. De & Erra, U.) (The Eurographics Association, 2008). doi:10.2312/LocalChapterEvents/ItalChap/ItalianChapConf2008/129-136.

35. Buffrénil, V. de & Schoevaert, D. Données quantitatives et observations histologiques sur la pachyostose du squelette du dugong, *Dugong dugon* (Müller) (Sirenia, Dugongidae). *Can. J. Zool.* **67**, 2107–2119 (1989).

36. Domning, D. P. Sirenian evolution in the North Pacific Ocean. *Univ. Calif. Publ. Geol. Sci.* **118**, 1–176 (1978).

37. Sarko, D. K., Domning, D. P., Marino, L. & Reep, R. L. Estimating body size of fossil sirenians. *Mar. Mammal Sci.* **26**, 937–959 (2010).

38. Boschian, G., Caramella, D., Saccà, D. & Barkai, R. Are there marrow cavities in Pleistocene elephant limb bones, and was marrow available to early humans? New CT scan results from the site of Castel di Guido (Italy). *Quat. Sci. Rev.* **215**, 86–97 (2019).

39. Larramendi, A. Proboscideans: Shoulder Height, Body Mass and Shape. *Acta Palaeontol. Pol.* **56**, 463–475 (2015).

40. Buffrénil, V. de. Contribution à l'étude des spécialisations de la structure osseuse des mammifères marins. (Thèse de doctorat ès sciences, Université Paris VII , Paris, 1990).

41. O'Flaherty, E. J. Physiologically based models for bone-seeking elements. I. Rat skeletal and bone growth. *Toxicol. Appl. Pharmacol.* **111**, 299–312 (1991).

42. Lockyer, C. Body weights of some species of large whales. *ICES J. Mar. Sci.* **36**, 259–273 (1976).

43. Tacutu, R. *et al.* Human Ageing Genomic Resources: Integrated databases and tools for the biology and genetics of ageing. *Nucleic Acids Res.* **41**, D1027–D1033 (2013).

44. Meiri, S. Length weight allometries in lizards. *J. Zool.* **281**, 218–226 (2010).

45. Glaw, F. *et al.* Extreme miniaturization of a new amniote vertebrate and insights into the evolution of genital size in chameleons. *Sci. Rep.* **11**, 1–14 (2021).

46. Stein, K. & Sander, P. M. Histological Core Drilling: a Less Destructive Method for Studying Bone Histology. *Methods Foss. Prep. Proc. First Annu. Foss. Prep. Collect. Symp.* 69–80 (2009).

47. Martínez-Cáceres, M., Lambert, O. & Muizon, C. de. The anatomy and phylogenetic affinities of *Cynthiacetus peruvianus*, a large *Dorudon*-like basilosaurid (Cetacea, Mammalia) from the late Eocene of Peru. *Geodiversitas* **39**, 7–163 (2017).

48. Blender Online Community. Blender - a 3D modelling and rendering package. at http://www.blender.org (2018).

49. Gingerich, P. D., Smith, B. H. & Simons, E. L. Hind limbs of Eocene *Basilosaurus*: evidence of feet in whales. *Science* **249**, 154–157 (1990).

50. Uhen, M. D. Form, function, and anatomy of *Dorudon atrox* (Mammalia, Cetacea): an archaeocete from the middle to late Eocene of Egypt. *Univ. Michigan Pap. Paleontol.* **34**, 1–222 (2004).

51. Gingerich, P. D., Amane, A. & Zouhri, S. Skull and partial skeleton of a new pachycetine genus (Cetacea, Basilosauridae) from the Aridal Formation, Bartonian middle Eocene, of southwestern Morocco. *PLoS One* **17**, 1–43 (2022).

52. Uhen, M. D. New material of eocetus wardii (mammalia,cetacea) from the middle eocene of North Carolina. *Southeast. Geol.* **40**, 135–148 (2001).

53. Houssaye, A., Tafforeau, P., Muizon, C. de & Gingerich, P. D. Transition of Eocene whales from land to sea: evidence from bone microstructure. *PLoS One* **10**, e0118409 (2015).

54. Uhen, M. D. New species of protocetid archaeocete whale, *Eocetus wardii* (Mammalia: Cetacea) from the middle Eocene of North Carolina. *J. Paleontol.* **73**, 512–528 (1999).

55. Buffrénil, V. de, Ricqlès, A. de, Ray, C. E. & Domning, D. P. Bone histology of the ribs of the archaeocetes (Mammalia: Cetacea). *J. Vertebr. Paleontol.* **10**, 455–466 (1990).

56. Buffrénil, V. de & Lambert, O. Histology and growth pattern of the pachy-osteosclerotic premaxillae of the fossil beaked whale *Aporotus recurvirostris* (Mammalia, Cetacea, Odontoceti). *Geobios* **44**, 45–56 (2011).

57. Gol'din, P. & Zvonok, E. *Basilotritus uheni*, a new cetacean (Cetacea, Basilosauridae) from the late middle Eocene of eastern Europe. *J. Paleontol.* **87**, 254–268 (2013).

58. Dewaele, L. *et al.* Generalized osteosclerotic condition in the skeleton of *Nanophoca vitulinoides*, a dwarf seal from the Miocene of Belgium. *J. Mamm. Evol.* **26**, 517–543 (2019).

59. Houssaye, A., Martin Sander, P. & Klein, N. Adaptive patterns in aquatic amniote bone microanatomy—more complex than previously thought. *Integr. Comp. Biol.* **56**, 1349–1369 (2016).

60. Dewaele, L. *et al.* Hypersalinity drives convergent bone mass increases in Miocene marine mammals from the Paratethys. *Curr. Biol.* **32**, 248-255.e2 (2022).

61. Tarasenko, K. K. A New Seal Species of the Genus *Pachyphoca* (Cystophorinae, Phocidae) from the Late Miocene of the North Caucasus. *Dokl. Earth Sci.* **507**, 916–919 (2022).

62. Buffrénil, V. de, Canoville, A., D'Anastasio, R. & Domning, D. P. Evolution of sirenian pachyosteosclerosis, a model-case for the study of bone structure in aquatic tetrapods. *J. Mamm. Evol.* **17**, 101–120 (2010).

Supplementary Tables

Supplementary Table 1. *Perucetus colossus'* holotype (MUSM 3248) measurements.

Vertebrae	Th-a	Th-b	L-a	L-b	L-c	L-d	L-e	L-f	L-g	L-h	L-i	L-j	L-k
Maximum ML width (cm)	70†	78	84	84†	89	89	88	86	-	82	-	80	80
Maximum DV height (cm)	61	68	71	-	69†	74	-	-	-	61	-	70	70
Centrum, AP length (cm)	32	31*	35*	35*	33*	36	35	30†	-	-	-	32*	31
Centrum, anterior ML width (cm)	22	25	23	23†	24	24	24	25†	-	-	-	22	22
Centrum, anterior DV height (cm)	19	23	21	20†	21	21	18	20†	-	-	-	19	18
Centrum, posterior ML width (cm)	23	24	25	24	25	24	24	23	-	24	-	23	23
Centrum, posterior DV height (cm)	20	21	21	20	20	20	19	21	-	20	-	19	18
Neural canal, Anterior ML width (cm)	14	16	17	-	19	18	18	16	-	-	-	20	19
Neural canal, anterior DV height (cm)	5	5	6	-	7	6	-	-	-	-	-	6	5
Neural canal, posterior ML width (cm)	14	18	17	-	20	19	19	19	-	20	-	24	23
Neural canal, posterior DV height (cm)	6	4	6	-	7	7	-	-	-	8	-	7	7
Whole volume (dm^3)	-	60	74	-	-	81	-	-	-	-	-	69	63

Supplementary Table 1. (continued).

Rib	R-a
Chord (cm)	11.0
PD length (along the curvature; cm)	13.5
Whole volume (dm^3)	16
Innominate	
Greatest vertical diameter (mm)	113
Vertical diameter at the level of the maximal vertical diameter of the obturator foramen (mm)	77
Acetabulum, vertical diameter (mm)	40
Acetabulum, transverse diameter (mm)	37
Obturator foramen, vertical diameter (mm)	21
Obturator foramen, vertical diameter (mm)	44

Footnotes.
Abbreviations: AP, anteroposterior; DV, dorsoventral; ML, mediolateral; PD, proximodistal.

*, reconstructed adding centrum epiphysis thickness; †, estimated

Supplementary Table 2. Bone global compactness (ratio of bone tissue area versus total cross-sectional area) in rib cross-section and vertebral cores of *Perucetus colossus*, along with other mammals for comparison.

		Rib midshaft	Centrum (DV)	NS	TP	Sources
	Perucetus colossus†	0.995	0.674*	0.983	0.838	**This study**
Other basilosaurids	*Basilosaurus* sp.†	0.879				Houssaye et al. (2015)
	Dorudon atrox†	0.858				Houssaye et al. (2015)
Cetaceans from Paratethys	*Pachyacanthus suessii*†	0.999				Dewaele at al. (2021)
	Brandtocetus chongulek†	ca. 1.000				Dewaele at al. (2021)
	Cetotheriidae indet.†	0.998				Dewaele at al. (2021)
Extant cetaceans	Delphinoidea	0.416-0.879	0.307	0.664	0.792	Buffrénil et al. (2010); Canoville, et al. (2016);**This study**
	Inia goeffrensis	0.365	0.43	0.614	0.75	Canoville, et al. (2016)
	Mesoplodon densirostris	0.264				Canoville, et al. (2016)
	Balaena mysticetus	0.59-0.67*				George et al. (2016)
	Balaenoptera brydei	0.665				Hayashi et al. (2013)
	Balaenoptera acutorostrata	-	0.475	0.663	-	This study

Supplementary Table 2. (continued).

		Rib midshaft	Centrum (DV)	NS	TP	Sources
Sirenians	*Pezosiren portelli*†	0.755				Buffrénil et al. (2010)
	Trichechus manatus	0.985	0.407	0.896	0.616	Buffrénil et al. (2010);**This study**
	Dugong dugon	0.977	0.378	0.697		Buffrénil et al. (2010);**This study**
	All other sirenians combined	0.949-0.999				Buffrénil et al. (2010)

Footnotes:
Abbreviations: DV, dorsoventral; NR, neural spine; TP, transverse process.
*The global compactness value for the centrum of *P. colossus* was obtained by averaging the measurements for the eleven zones of the core drill (taking into account the proportion of the centrum radius sampled with the ten zones, i.e., 74%; see Supplementary Table 19).

Supplementary Table 3. Scaling of the skeletal mass versus whole body mass in extant, terrestrial mammals (n = 40 species). Phylogenetically informed Generalised Least Squares (PGLS) regressions rely on the optimised Pagel's lambda. To test for allometry (expected slope under isometry here is 1), another regression subtracting the BM to the SM was performed.

GLS fit by maximum likelihood. Model: log10(SkeletalMass) ~ log10(BodyMass) AIC: -89.58; BIC: -84.51; logLik: 47.79 Estimated lambda: 0 Pseudo R^2: 0.997 Shapiro.test(Residuals): W = 0.97473, p-value (one-sided) = 0.5011				
	Value	Std.Error	t-value	p-value (two-sided)
(Intercept)	-1.25	0.01	-89.40	8.63e-46
log10(BodyMass)	1.03	0.01	119.66	**1.39e-50**
Isometry? GLS fit by maximum likelihood. Model: log10(SkeletalMass) - log10(BodyMass) ~ log10(BodyMass)				
	Value	Std.Error	t-value	p-value (two-sided)
(Intercept)	-1.25	0.01	-89.40	8.63e-46
log10(BodyMass)	0.03	0.01	3.59	**9.30e-04**

Supplementary Table 4. Scaling of the skeletal mass versus whole body mass in extant cetaceans (n = 14 species). Methods as in Supplementary Table 3.

GLS fit by maximum likelihood. Model: log10(SkeletalMass) ~ log10(BodyMass) AIC: -25.73; BIC: 23.81; logLik: 15.86 Estimated lambda: 1 Pseudo R^2: 0.99 Shapiro.test(Residuals): W = 0.90149, p-value (one-sided) = 0.1186				
	Value	Std.Error	t-value	p-value (two-sided)
(Intercept)	-1.49	0.12	-12.42	3.28e-08
log10(BodyMass)	1.01	0.03	31.93	**5.62e-13**
Isometry? GLS fit by maximum likelihood. Model: log10(SkeletalMass) - log10(BodyMass) ~ log10(BodyMass)				
	Value	Std.Error	t-value	p-value (two-sided)
(Intercept)	-1.49	0.12	-12.42	3.28e-08
log10(BodyMass)	0.01	0.03	0.41	0.69

Supplementary Table 5. ^{39}Ar-^{40}Ar step-heating results of the biotite separate. All isotopes are in ml; ages are in Ma.

Step	T (°C)	^{40}Ar total	Err. ^{40}Ar	$^{40}Ar^*$	^{39}Ar	Err. ^{39}Ar	% ^{39}Ar	^{38}Ar	Err. ^{38}Ar	$^{38}Ar_{Cl}$	^{37}Ar	Err. ^{37}Ar
1	706	4.36E-08	1.80E-11	6.13E-10	3.94E-11	2.81E-13	1.93	1.10E-10	1.20E-13	8.23E-11	3.36E-12	2.06E-13
2	845	2.71E-08	9.59E-12	5.22E-09	2.06E-10	3.19E-13	10.11	3.97E-11	4.48E-14	2.35E-11	5.94E-12	2.06E-13
3	913	8.71E-09	1.33E-12	6.16E-09	2.41E-10	3.46E-13	11.82	3.02E-11	3.35E-14	2.57E-11	1.12E-12	2.06E-13
4	994	1.18E-08	2.25E-12	9.20E-09	3.62E-10	4.10E-13	17.75	4.37E-11	4.76E-14	3.78E-11	1.28E-12	2.06E-13
5	1036	1.12E-08	2.25E-12	8.19E-09	3.23E-10	3.39E-13	15.84	3.93E-11	4.37E-14	3.36E-11	1.75E-12	2.06E-13
6	1076	9.46E-09	1.87E-12	4.76E-09	1.89E-10	3.61E-13	9.25	2.54E-11	3.02E-14	2.02E-11	2.12E-12	2.06E-13
7	1109	8.73E-09	1.64E-12	4.18E-09	1.65E-10	3.13E-13	8.10	2.27E-11	2.78E-14	1.79E-11	2.17E-12	2.06E-13
8	1132	6.95E-09	1.38E-12	3.90E-09	1.55E-10	3.12E-13	7.59	1.99E-11	2.43E-14	1.61E-11	2.05E-12	2.06E-13
9	1167	5.04E-09	9.13E-13	3.41E-09	1.35E-10	3.33E-13	6.61	1.62E-11	2.07E-14	1.36E-11	1.98E-12	2.06E-13
10	1288	8.33E-09	1.71E-12	5.68E-09	2.24E-10	3.43E-13	10.99	2.55E-11	3.15E-14	2.12E-11	6.41E-12	2.07E-13

Supplementary Table 5. (continued).

Step	^{36}Ar	Err. ^{36}Ar	Age	Error age	Ca/K	Err. Ca/K	Cl/K	Err. Cl/K	$^{39}Ar/^{40}Ar$	Err. $^{39}Ar/^{40}Ar$	$^{36}Ar/^{40}Ar$	Err. $^{36}Ar/^{40}Ar$
1	1.44E-10	2.80E-13	22.48	3.14	0.1657	0.0102	0.3719	0.0027	9.03E-04	6.45E-06	3.30E-03	6.55E-06
2	7.32E-11	1.41E-13	36.47	0.31	0.0559	0.0019	0.0203	0.0000	7.62E-03	1.21E-05	2.70E-03	5.29E-06
3	8.53E-12	1.99E-14	36.77	0.06	0.0090	0.0017	0.0190	0.0000	2.77E-02	3.99E-05	9.80E-04	2.29E-06
4	8.86E-12	2.04E-14	36.57	0.05	0.0069	0.0011	0.0186	0.0000	3.06E-02	3.51E-05	7.48E-04	1.72E-06
5	9.97E-12	2.18E-14	36.48	0.05	0.0105	0.0012	0.0185	0.0000	2.89E-02	3.09E-05	8.92E-04	1.96E-06
6	1.57E-11	3.23E-14	36.34	0.10	0.0218	0.0021	0.0190	0.0000	2.00E-02	3.84E-05	1.66E-03	3.44E-06
7	1.52E-11	3.14E-14	36.43	0.11	0.0255	0.0024	0.0192	0.0000	1.89E-02	3.61E-05	1.74E-03	3.62E-06
8	1.02E-11	2.30E-14	36.24	0.10	0.0257	0.0026	0.0185	0.0001	2.23E-02	4.51E-05	1.47E-03	3.32E-06
9	5.46E-12	1.38E-14	36.38	0.10	0.0285	0.0030	0.0180	0.0001	2.68E-02	6.63E-05	1.08E-03	2.75E-06
10	8.89E-12	2.08E-14	36.44	0.07	0.0554	0.0018	0.0168	0.0000	2.69E-02	4.16E-05	1.07E-03	2.51E-06

Supplementary Table 6. Large cetacean skeletal and whole body mass estimations.

	SMm	TL	SF	BMe_a	BMe_b	**BMe**	BMm	**SMe**
Balaenoptera musculus (Wexford blue whale; NHMUK ZD.1892.3.1.1.)	2.65E+03	2.52E+01		0.002899	3.25	1.04E+05		-
Balaenoptera musculus (adult male. A. 5805; Robineau and Buffrénil 1993)	2.96E+03	2.33E+01	3.68E-02	0.002899	3.25	8.05E+04		
Balaenoptera musculus (species mean; AnAge)	-						1.36E+05	5.00E+03
Physeter macrocephalus (juvenile. A. 5681; Robineau and Buffrénil 1993)	1.67E+03	1.45E+01	5.07E-02	0.006648	3.18E+00	3.29E+04		-
Physeter macrocephalus (species mean; AnAge)							2.85E+04	1.44E+03

Footnotes:
SMm: whole skeletal mass (kg), measured
SMe, whole skeletal mass (kg), estimated (this study)
BMe, BMe_a, BMe_b: body mass (kg), estimated with equations of Lockyer (1976), given the constants a and b
BMm, body mass (kg), species mean (AnAge database)
TL: Total length (m)
SF: Skeletal fraction (no units)

Supplementary Table 7. *Diplodocus*, skeletal mass estimations based on the specimen CM 84 (data from Larramendi et al., 2021).

	V	Dw	Md	Dd	Compact bone %	Dw	Dd	DredMarrow	Dtrab
Skull (apneumatic)	4.76E-03	1.50E+03	6.78E+00	1.43E+03					
Cervicals (pneumatic)	8.42E-02	1.90E+03	1.52E+02	1.81E+03					
Dorsals (pneumatic)	9.95E-02	1.90E+03	1.80E+02	1.81E+03					
Sacrals (pneumatic)	3.04E-02	1.90E+03	5.49E+01	1.81E+03					
Ribs (pneumatic; Air Space Proportion (ASP9 = 0.6	3.87E-02	1.90E+03	6.99E+01	1.81E+03					
Appendicular trunk (ilium, ischion, pubis; apneumatic)	3.00E-01	1.50E+03	4.27E+02	1.43E+03					
Skeletal forelimb	7.50E-02	1.65E+03	9.05E+01	1.21E+03	6.45E-01	1.90E+03	1.81E+03	1.03E+03	1.15E+03
Skeletal hind limb	1.80E-01	1.65E+03	2.17E+02	1.21E+03	6.45E-01	1.90E+03	1.81E+03	1.03E+03	1.15E+03
Anterior caudal (pneumatic)	1.06E-01	1.90E+03	1.91E+02	1.81E+03					
Mid-posterior caudals (apneumatic)	7.14E-02	1.90E+03	1.29E+02	1.81E+03					
Whole skeleton	9.89E-01		1.52E+03						

Footnotes:
V: volume (m3)
Mw: Wet skeletal mass (kg)
Dw: density corresponding to wet skeleton (kg.m-3)
Md: Dry skeletal mass (kg)
Dd: density (kg.m-3) corresponding to dry compact bone (including small porosity)
Compact bone %, percentage of compact bone (limb elements)
DredMarrow: density of red marrow (kg.m-3)
Dtrab: density of dry trabecular bone (kg.m-3)

Supplementary Table 8. Extrapolation of *Diplodocus*' skeletal mass estimations to *Argentinosaurus huinculensis* (PVPH 1).

	BMe	BMe_min	BMe_max	SF	**SMe**	SMe_min	SMe_max
Diplodocus (CM 84)	1.45E+04			1.05E-01			
Argentinosaurus huinculensis (PVPH 1)	9.47E+04	7.04E+04	1.19E+05		9.93E+03	7.39E+03	1.25E+04

Footnotes:
BMe, BMe_min, BMe_max: body mass (kg) with minimum and maximum estimates (Campione and Evans 2020)
SF: Skeletal fraction (no units)
SMe, SMe_min, SMe_max: whole skeletal mass (kg) with minimum and maximum estimates (this study)

Supplementary Table 9. Small-bodied amniotes skeletal and whole body mass estimations.

	SV	Dd	**SM**	BMm	SVL	BMe_a	BMe_b	**BMe**
Suncus etruscus (SMNS-Z-MAM-49066)	5.94E-08	1.89E+03	1.12E-04	2.10E-03				
Brookesia nana (UADBA-R/FGZC 3752)	1.40E-08	1.89E+03	2.64E-05		1.92E+01	-3.99E+00	2.68E+00	2.81E-04
Sphaerodactylus sputator (ummz-herps-174801)	2.06E-08	1.89E+03	3.90E-05		2.90E+01	-4.50E+00	2.90E+00	5.58E-04

Footnotes:
SV: skeleton volume (m3), segmented on CT-scans
Dd: mean dry bone tissue density (kg.m-3) (based on *Panthera leo)*
BMm, body mass (kg), measured
SVL: snout-vent length (mm)
BMe, BMe_a, BMe_b: body mass (kg), estimated with equations of Meiri (2010), given the constants a and b
SM: whole skeletal mass (kg), estimated (this study)

Supplementary Table 10. Estimation of *Dugong dugon*'s skull and mandible density, as to mimic a surface model.

	Vb	Dd	M	Vm	**D**
NHMUK 2005-51	1.86E-03	2120	3.95E+00	2.42E-03	1.63E+03

Footnotes:
Vb: volume of bone (m3), both skull and mandible
Dd: *D. dugon* mean dry bone tissue density (kg.m-3)
M: mass (kg)
Vm: Volume of corresponding mesh (Screened Poisson Reconstruction)
D: overall density (kg.m-3)

Supplementary Table 11. Estimation of *Dugong dugon*'s skeleton density.

***Dugong dugon* skeletal density**	Skull and Mandible	Forelimb	Sacrum	Ribs	Vertebrae	Overall skeleton
Mass*	4.62E+00	1.58E+00	1.40E-01	7.45E+00	6.51E+00	2.03E+01
Relative Mass*	2.28E-01	7.79E-02	6.90E-03	3.67E-01	3.21E-01	
Density**	1.63E+03	1.63E+03	2.00E+03	2.06E+03	9.41E+02	
Overall density	3.72E+02	1.27E+02	1.38E+01	7.57E+02	3.02E+02	1.57E+03

Footnotes:
*Based on *D. dugon* (SMNS-Z-MAM-1288)

**Based on Buffrénil & Schoevaert (1989) adult specimen's data except for skull and mandible (see above)

Supplementary Table 12. Extinct sirenian skeletal and whole body mass estimations.

	Vm	**SMe**	BSL	BLm	BLe_a	BLe_b	BLe	BMe_a	BMe_b	**BMe**	BMe_min_a	BMe_min_b	**BMe_min**	BMe_max_a	BMe_max_b	**BMe_max**
Kaupitherium bronni SMNS-P-47736	4.27E-02	6.70E+01	3.13E-01	-	-	-	-	-3.704	4.084	2.53E+02	-3.53	3.87E+00	1.79E+02	-3.663	4.086	2.80E+02
Hydrodamalis gigas (NHMW-Zoo-MAMM 614)	2.86E-01	4.50E+02	6.44E-01	6.2	-	-	-	-3.704	4.084	4.83E+03	-3.53	3.87E+00	2.92E+03	-3.663	4.086	5.36E+03
Hydrodamalis cuestae (LACM 25917)	-	1.37E+03	8.30E-01		0.357	1.353	8.98	-3.704	4.084	1.36E+04	-3.53	3.87E+00	7.78E+03	-3.663	4.086	1.51E+04

Footnotes:
Vm: volume of skeleton model (m3)
SMe, whole skeletal mass (kg), estimated
BSL: condylobasal skull length (m)
BLm: body length (m), measured
BLe, _a, _b, body length (m), estimated with the BSL-based equation of Sarko et al. (2010), given the constants a and b
BMe, _a, _b, _min, _max: intermediate, minimum, and maximum body mass estimates (kg), with BSL-based equations of Sarko et al. (2010), given the constants a and b

Supplementary Table 13. Large proboscidean long bone density, based on *Palaeoloxodon antiquus*, following Larramendi (2015).

	CBV	Dd	SBV	DredMarrow	Dtrab	Dsb	**Density femur**
Palaeoloxodon antiquus, CdG29 (Boschian et al. 2019)	2.53E+04	1.89E+03	1.23E+04	1.03E+03	1.15E+03	1.20E+02	1.30E+03

Footnotes:
CBV: compact bone volume (cm3)
Dd: mean dry bone tissue density (kg.m-3) (based on *Panthera leo*)
SBV: spongy bone volume (cm3)
DredMarrow: density of red marrow (kg.m-3)
Dtrab: density of dry trabecular bone (kg.m-3)
Dsb: spongy bone density, including intertrabecular space (kg.m-3)

Supplementary Table 14. *Panthera leo*'s skeletal element density estimations based on mass and surface model volume.

	V	M	D
Skull (SMNS-Z-MAM-49240)	2.06E-03	1.20E+00	5.82E+02
Mandible (SMNS-Z-MAM-49240)	4.02E-04	5.60E-01	1.39E+03
Pelvis (SMNS-Z-MAM-2055)	5.92E-04	6.50E-01	1.10E+03
Foot (SMNS-Z-MAM-2055)	3.30E-04	4.30E-01	1.30E+03

Footnotes:
V: volume (m3)
M: mass (kg)
D: density (kg.m-3)

Supplementary Table 15. Estimation of *Panthera leo*'s skeletal element density (without long bones).

	M	Mr	D	Dr
Skull*	1.19E+00	1.96E-01	5.82E+02	1.14E+02
Mandible*	5.20E-01	8.58E-02	1.39E+03	1.20E+02
Hand	4.80E-01	7.92E-02	1.34E+03	1.06E+02
Scapula	4.40E-01	7.26E-02	8.90E+02	6.46E+01
Sternum	6.00E-02	9.90E-03	4.30E+02	4.26E+00
Ribs	6.30E-01	1.04E-01	1.14E+03	1.19E+02
Vertebrae	1.53E+00	2.52E-01	8.55E+02	2.16E+02
Pelvis*	2.49E+00	4.11E-01	1.10E+03	4.51E+02
Foot*	4.30E-01	7.92E-02	1.30E+03	1.06E+02
Total	6.06E+00			1.30E+03

Footnotes:
*, own density estimations based on SMNS-Z-MAM-49240 (skull and mandible) and SMNS-Z-MAM-2055 (pelvis and foot); the rest is taken from Buffrénil et al. (1986)
M: mass (kg)
Mr: relative mass (no units)
D: density (kg.m-3)
Dr: relative density (no units)

Supplementary Table 16. *Prodeinotherium* skeletal mass estimation.

	SV	HlV	FlV	**SMe**
***Prodeinotherium* (NHMW2000z0047/0001)**	3.51E-01	3.12E-02	3.05E-02	4.56E+02

Footnotes:
SV: skeleton volume (m3)
HlV: hindlimb long bones volume (m3)
HlV: forelimb long bones volume (m3)
SMe: skeletal mass estimate (kg), using *P. antiquus* femoral density for long bones and mean values of *Panthera leo* for the rest

Supplementary Table 17. Scaling of the vertebral column of Cy*nthiacetus peruvianus*' holotype to *Perucetus colossus'* dimensions. Measurements are in millimetres.

	Width	Height	Length
***C. peruvianus* (MNHN.F.PRU10)**			
T17-T20 (2 vertebrae)	278.69	249.65	257.95
L1-17 (8 vertebrae)	1260.93	1236.29	1122.03
All (10 vertebrae)	1539.62	1485.94	1379.97
***P. colossus* (MUSM 3248)**			
T17-T20 (2 vertebrae)	472	417	635
L1-17 (8 vertebrae)	1879	1573	2657.5
All (10 vertebrae)	2351	1990	3292.5
General ratio	1.53	1.34	2.39

Supplementary Table 18. Dilating the 3D model of Cy*nthiacetus peruvianus*' holotype (MNHN.F.PRU10) to *P. colossus'* volume. Volumes are in cubic metres.

	Vertebrae	Ribcage	Skull and mandible	Girdles and limbs	Whole skeleton
Initial model volume (*C. peruvianus*)	0.1211	0.0216	0.0301	0.0054	0.1782
Scaled-up volume (no pachyostosis)	0.5935	0.2773/0.4854*	0.088	0.0156	0.9744/1.1825*
Scaled-up, inflated volume	2.7241	0.8689/1.2755*	0.088	0.0156	3.6966/4.1032*
***Basilosaurus isis* version**	2.7803	0.8033/1.1798*	0.088	0.0156	3.6872/4.0637*
***Dorudon atrox* version**	2.7985	0.7707/1.1322*	0.088	0.0156	3.6728/4.0343*
Conservative count version**	2.2735	0.5431	0.088	0.0156	2.9202/3.1762*

Footnotes:

*, the two values correspond to the estimation using as a base the 17th and 20th rib of *C. peruvianus*, respectively.

**, 12 thoracic segments and 15 lumbar vertebrae (see above).

Supplementary Table 19. Overall global compactness of the vertebral parts (centrum, neural arch, and transverse processes) of *Perucetus colossus* assessed with core drills. See Extended Data Fig. 7a1-3 for the centrum dorsoventral, neural arch, and transverse process core drills, respectively, and see Supplementary Fig. S12 for the centrum posteroanterior core drill.

			S	V	C	V*C
Centrum						
	Dorsoventral core areas (L-e)	1 (external)	5.17E+03	1.48E+06	9.99E-01	1.48E+06
		2	4.80E+03	1.38E+06	9.98E-01	1.37E+06
		3	4.43E+03	1.27E+06	9.98E-01	1.27E+06
		4	4.06E+03	1.17E+06	1.00E+00	1.17E+06
		5	3.70E+03	1.06E+06	9.97E-01	1.06E+06
		6	3.33E+03	9.55E+05	8.57E-01	8.18E+05
		7	2.96E+03	8.49E+05	7.51E-01	6.38E+05
		8	2.59E+03	7.44E+05	4.18E-01	3.11E+05
		9	2.23E+03	6.38E+05	4.18E-01	2.67E+05
		10 (internal)	1.86E+03	5.33E+05	3.73E-01	1.99E+05
	Dorsoventral core, added area	11 (innermost)	3.63E+03	1.04E+06	3.73E-01	3.89E+05

Supplementary Table 19. (continued).

			S	V	C	V*C
	Posteroanterior core areas (Th-a)	1 (external)	3.36E+04	2.19E+05	7.65E-01	1.68E+05
		2	3.36E+04	2.19E+05	8.40E-01	1.84E+05
		3	3.36E+04	2.19E+05	8.79E-01	1.93E+05
		4	3.36E+04	2.19E+05	6.44E-01	1.41E+05
		5	3.36E+04	2.19E+05	6.98E-01	1.53E+05
		6	3.36E+04	2.19E+05	7.27E-01	1.59E+05
		7	3.36E+04	2.19E+05	6.06E-01	1.33E+05
		8	3.36E+04	2.19E+05	5.21E-01	1.14E+05
		9	3.36E+04	2.19E+05	4.43E-01	9.70E+04
		10 (internal)	3.36E+04	2.19E+05	5.18E-01	1.13E+05
	Whole centrum		-	1.33E+07	**7.83E-01**	1.04E+07
Neural arch core drill (L-c)			-	-	**9.83E-01**	-
Transverse process core drill (L-e)			-	-	**8.38E-01**	-

Footnotes:

S: for the dorsoventral core areas, S is the surface of the concentric zones of an ellipsoid, to which the shape of the centrum (mediolateral width: 235 mm; dorsoventral height: 210 mm) was assimilated; for the posteroanterior core areas, S is an elliptical surface corresponding to the dimensions of the posterior face of the centrum: 235*182 mm. See Supplementary Methods and R script (https://github.com/eliamson/ColossalCode). Unit: mm^2

V: extrapolation of the former to the corresponding volume of the centrum. For the dorsoventral core, this corresponds to the product with the centrum anteroposterior length (352 mm) minus the length of the posteroanterior core (32.6 mm) times two. For the posteroanterior core, S was multiplied by a tenth of the length of the posteroanterior core times two. Unit: mm^3

C: global compactness (surface occupied by bone/total surface). It is either measured in each of the core drills' zones (for the centrum cores, see also Extended Data 8 and Fig. S12), whole core drills (for the neural arch or transverse process), or the result of the whole centrum's V*C (see below) divided by the whole centrum's V. No units.

V*C: product of the former two, used to compute the overall global compactness of the centrum. Units: mm^3.

Supplementary Table 20. Vertebral column overall compactness of *Perucetus colossus* based on proportions of the vertebral parts (centrum, neural arch, and transverse processes) in *C. peruvianus* (MNHN.F.PRU10) and their respective global compactness values.

	C_Centrum	C_Neural arch	C_Transverse process	Vp_centrum	VpNeural arch	Vp_Transverse process	Overall_C
P. colossus, single vertebra	7.83E-01	9.83E-01	8.38E-01				-
C. peruvianus, whole column	-	-	-	7.80E-01	1.40E-01	8.03E-02	
P. colossus's, whole column	-	-	-	3.15E-01	3.10E-01	3.85E-01	**8.77E-01**

Footnotes:
C_Centrum, C_neural arch, C_Transverse process: global compactness of the respective vertebral parts (see Supplementary Table 19).
Vp_centrum, VpNeural arch, Vp_Transverse process: relative volume of the respective vertebral parts within a whole vertebral column (see Supplementary Data 4). This was measured with a 3D model for *C. peruvianus*, or, for *P. colossus,* estimated based on the ratio between *C. peruvianus'* proportions and those measured with the 3D models of the complete enough vertebrae of *P. colossus,* i.e., 0.24 for the centrum, 2.22 for the neural arch, and 4.80 for the transverse processes (see also Supplementary Methods and R code at https://github.com/eliamson/ColossalCode).
Overall_C: overall global compactness of the whole vertebral column.
All without units. Note that the total of *P. colossus* parts' proportions is below 1 because of the difference of relative proportions along the column.

Supplementary Table 21. *Delphinus delphis* (SMNS-Z-MAM-41077) skull and mandible density.

	Skull	Mandible	Overall
Mesh Volume (cm3)	1741.156	92.370	
mass (g)	740	160	
density (g.cm-3)	0.425	1.732	0.491

Supplementary Table 22. *Perucetus colossus* skeletal and whole body mass estimations.

	SV	Dd	Sd	Ld	Cg	**SM**	SF	**BM**
Minimum estimate*								
Vertebrae	2.27E+00	2.07	-	-	8.77E-01	4.13E+03	-	-
Ribcage	5.43E-01	2.07	-	-	9.95E-01	1.12E+03		
Head	8.80E-02	-	4.91E-01	-	-	4.32E+01		
Limbs	1.56E-02	-	-	8.46E-01	-	1.32E+01		
All	2.92E+00		-	-	-	**5.30E+03**	6.25E-02	**8.49E+04**
Maximum estimate**								
Vertebrae	2.72E+00	2.07	-	-	8.77E-01	4.95E+03	-	-
Ribcage	1.28E+00	2.07	-	-	9.95E-01	2.63E+03	-	-
Head	8.80E-02	-	4.91E-01	-	-	4.32E+01	-	-
Limbs	1.56E-02	-	-	8.46E-01	-	1.32E+01	-	-
All	4.10E+00	-	-	-	-	**7.63E+03**	2.24E-02	**3.41E+05**

Footnotes:

Dd: mean dry bone tissue density ($kg.m^{-3}$) (based on *Delphinus delphis*)

Sd: skull overall density ($kg.m^{-3}$) (based on *Delphinus delphis*)

Ld: mean limb bone density ($kg.m^{-3}$) (based on *Delphinus delphis*; Buffrénil et al. 1986)

Cg: global compactness, this study (no units)

SM: skeletal mass (kg)

SF: Skeletal fraction (no units) of *Trichechus manatus* (mean of adults, based on Domning & Buffrénil 1991) for the minimum estimate, and *Mesoplodon europaeus* (Robineau & Buffrénil, 1993) for the maximum estimate

BM: body mass (kg)

*, using the conservative skeleton composition with R17 as the corresponding rib (see above)

**, using *Cynthiacetus peruvianus* skeletal composition, with R20 as the corresponding rib (see above)